Development of a functional magnetic resonance imaging simulator: Deterministic simulation of the transverse magnetization in microvasculature

Avery J. L. Berman, B.Sc.

Medical Physics Unit

McGill University, Montreal

July 2012

A thesis submitted to McGill University in partial fulfillment of the requirements of the degree of Master of Science

Abstract

Numerical simulations are invaluable in the development and understanding of magnetic resonance imaging (MRI) techniques. Motivated by the goal of understanding the behaviour of the functional MRI (fMRI) signal in brain tissue, this thesis employs a deterministic simulation technique in which the transverse magnetization and B_0 inhomogeneity within a voxel are spatially discretized and the stochastic self-diffusion of water molecules is modelled as a Gaussian isotropic blurring of the transverse magnetization. While this simulation technique has existed since fMRI was in its infancy, its use has increased recently as investigators have attempted to quantitatively interpret the measured signal. Despite its recent popularity, thorough quantitative validation of the technique is lacking in the literature.

With the development of quantitative fMRI techniques being the driving force, this thesis validates three-dimensional deterministic simulations of the MR signal with a focus on their application in cerebral microvasculature. Individual blood vessels are modelled by infinite cylinders with a realistic distribution of radii. Using a spin echo sequence, the effects of several simulation parameters are investigated.

Validations ignoring the effect of diffusion show that the discretization of the voxel into subvoxels can be very coarse – up to 10 μm subvoxel widths – without adversely affecting the simulation outcomes. Simulations including diffusion are validated using an analytical solution to the Bloch-Torrey equation for comparison. In the presence of diffusion, subvoxel size is a key factor and it needs to be sufficiently small (~ 2 μm), depending on the rest of the simulation parameters, in order for the simulations to be accurate. Finally, as a proof-of-concept, it is shown that larger subvoxels can be used and still produce accurate simulations if the diffusion coefficient is scaled by a correction factor to produce the desired time series.

Résumé

Les simulations numériques sont d'une valeur inestimable pour le développement et la compréhension des techniques d'imagerie par résonance magnétique (IRM). Cette thèse, motivée par le but de comprendre le comportement du signal de l'IRM fonctionnelle (IRMf) dans le tissu cérébral, utilise une technique de simulation déterministe dans laquelle la magnétisation transversale et l'inhomogénéité B0 au sein d'un voxel sont spatialement discrétisées et l'auto-diffusion stochastique des molécules d'eau est modélisée par un flou gaussien isotrope de la magnétisation transversale. Bien que cette technique de simulation existe depuis les débuts de l'IRMf, son utilisation a augmenté récemment par des chercheurs tentant d'interpréter quantitativement le signal mesuré. Malgré sa popularité récente, une validation quantitative approfondie de cette technique est absente de la littérature.

Ayant pour force motrice le développement de techniques d'IRMf quantitatives, cette thèse valide des simulations tridimensionnelles déterministes du signal IRM en mettant l'emphase sur leur application dans la microvascularisation cérébrale. Les vaisseaux sanguins individuels sont modélisés par des cylindres infinis avec une distribution de rayons réaliste. Les effets de plusieurs paramètres de simulation sont étudiées en utilisant une séquence écho de spin.

Des validations ignorant l'effet de diffusion montrent que la discrétisation des voxel en sous-voxels peut être très grossière - jusqu'à des tailles de sous-voxels de 10 μm - sans détériorer les résultats de la simulation. Des simulations tenant compte de la diffusion sont validées à l'aide d'une solution analytique à l'équation de Bloch-Torrey. En

présence de diffusion, la taille des sous-voxels est un facteur clé et doit être petite (~ 2 μm, dépendamment des autres paramètres de simulation) pour que les simulations soient précises. Enfin, comme preuve de concept, il est démontré que des simulations précises peuvent être obtenues avec des sous-voxels plus grands pourvu que le coefficient de diffusion soit multiplié par un facteur de correction pour produire la série temporelle désirée.

Contents

List of Figures

List of Tables

Glossary

ADC	apparent diffusion coefficient
ATP	adenosine triphosphate
B_0	static magnetic field
BOLD	blood oxygenation level-dependent
CBF	cerebral blood flow
CBV	cerebral blood volume
CMRGlc	cerebral metabolic rate of glucose
$CMRO_2$	cerebral metabolic rate of oxygen
CT	computed tomography
CVR	cerebrovascular resistance
D	diffusion coefficient
dCBV	deoxygenated cerebral blood volume
dHb	deoxyhemoglobin
EV	extravascular
FID	free induction decay
fMRI	functional MRI
GM	grey matter
Hct	hematocrit
IV	intravascular
M	calibration constant
MC	Monte Carlo
MRI	magnetic resonance imaging

M_{xy}	transverse magnetization
NMR	nuclear magnetic resonance
N_{ves}	number of vessels
OEF	oxygen extraction fraction
PET	positron emission tomography
R_2	transverse (spin-spin) relaxation rate
R_2'	reversible component of the transverse relaxation rate
R_2^*	apparent transverse relaxation rate
RF	radiofrequency
RMSE	root mean square error
S_bO_2	blood oxygen saturation
SDR	static dephasing regime
SE	spin echo
T_1	longitudinal (spin-lattice) relaxation time
T_2	transverse (spin-spin) relaxation time
T_2'	reversible component of the transverse relaxation time
T_2^*	apparent transverse relaxation time
t_c	characteristic time
TE	echo time
$\mathbf{V}$	vessel map
W	voxel width

τ_D	diffusive correlation time
[dHb]	concentration of deoxyhemoglobin
$\Delta\chi_{do}$	volume susceptibility difference between fully deoxygenated and fully oxygenated blood
Δx	subvoxel width
$\boldsymbol{\Delta\omega}$	frequency offset map
α	flow-volume coupling constant
β	intra/extravascular signal attenuation factor

γ	gyromagnetic ratio
δt	discrete time step
$\delta\omega$	characteristic frequency
ω_0	Larmor frequency
1D	one-dimensional
2D	two-dimensional
3D	three-dimensional

Acknowledgements

First and foremost, I would like to thank my supervisor, Dr. Bruce Pike, whose incredible support made this work possible for me. Bruce's guidance helped me persevere when stuck or wary and his encouragement of these simulations brought me real motivation.

Having undertaken a simulation-based thesis, I cannot thank the system administrators enough for their technical support. Specifically, I am indebted to Sylvain Milot for his incredible ability to sort out my problems and find solutions to them in such short time and helping me with the batch server – a task that saved me heaps of precious computing time. Similarly, I would like to thank Mike Ferreira for providing me with many helpful tips and pointers for running my simulations more smoothly and elegantly; Silvain Beriault for introducing me to the MATLAB library MEX, a tool that sped up my simulations enormously; Dr. Jen Campbell for useful discussions on diffusion and helping me root out a bug in my data analysis; Ilana Leppert, social organizer extraordinaire, whose nurturing guidance made our lab's daily operations run smoothly and with many smiles; and the rest of the member's of the MRI lab for their positive feedback on my project and making it such a joy to come into the lab.

Finally, I would like to thank my family for their continued support and my wonderful, loving girlfriend, Beth, who has unconditionally supported me in my studies, regardless of the circumstances, and always helps me see the bright side of things.

In addition, I would like to acknowledge financial support received from the Natural Sciences and Engineering Research Council of Canada (NSERC).

Chapter 1 Introduction

Magnetic resonance imaging (MRI) has revolutionized the way we look at the human body and, in particular, the brain. With its seemingly infinite number of potential contrast mechanisms, it has given us the ability to non-invasively image structural, functional, and metabolic features of the body without the risks associated with using ionizing radiation. Its ability to provide exquisite contrast of the body's soft tissues has made it an invaluable tool in medicine; this is one of the reasons a poll in 2001 of over 200 of the leading internists in the U.S. revealed that MRI and x-ray computed tomography (CT) scanning were considered the most important medical innovations for patients [1] and that the pioneers of MRI were awarded the Nobel Prize in Physiology or Medicine in 2003.

Despite MRI's widespread acceptance and use, it is far from being a completely understood system and there still are vast amounts of research being conducted on it as a technology and on its applications to health and life sciences. One such application is in

systems neuroscience, whose principal aim is to reveal how neural circuits and networks in the brain lead to perception, thought, and behaviour [2]. The work-horse of this field has been blood oxygenation level-dependent functional MRI (BOLD fMRI) [3-5]. Variations in the concentration of paramagnetic deoxyhemoglobin (dHb) in blood distort the local magnetic field, leading to an altered MR signal in the surrounding tissue. These variations in the concentration of dHb arise from a complex combination of hemodynamic and metabolic changes in the brain which themselves are triggered by neural activity (a process known as neurovascular coupling) [6-13]. BOLD imaging can therefore be used to infer changes in neural activity and localize it, allowing researchers to non-invasively map functional regions of the brain.

The ubiquity that functional MRI has seen in neuroscience has, unfortunately, still not been achieved in the clinic. A major reason for this being that BOLD fMRI is a largely qualitative imaging modality; it has the excellent ability to localize brain activity but its ability to quantify is severely limited. This is because, as mentioned above, the BOLD signal depends on the concentration of dHb, which is determined by *both* hemodynamic and metabolic changes, therefore preventing the independent measurement of either of these quantities. Consequently, in the clinic, where quantification of hemodynamic and metabolic responses in neurological diseases would be of significant value, fMRI has not been widely adopted.

To account for this, a wide array of functional imaging techniques has been developed to measure quantifiable physiological properties, such as cerebral blood flow (CBF) and blood volume (CBV), blood oxygen saturation (the fraction of hemoglobin in blood in the oxygenated state), oxygen extraction fraction (OEF; the ratio of O_2 used by the brain to the amount delivered by flowing blood), and the cerebral metabolic rate of oxygen ($CMRO_2$). Knowledge of these properties in a patient could significantly impact the patient's diagnosis and course of treatment. Additionally, certain neuropathologies, such as Alzheimer's disease [14] and stroke [15, 16], or pharmacological agents [17, 18] may dramatically alter neurovascular coupling such that BOLD images alone could suggest activation, deactivation, or nothing for a given functional response. By measuring $CMRO_2$ and CBF in the brain, the metabolic and hemodynamic changes can be

disentangled, allowing for an accurate assessment of the hemodynamic and neuroenergetic responses.

To gain further insights into the quantitative fMRI sequences developed for measuring the various physiological parameters, researchers often resort to computer simulations. Simulations permit the investigator to build a model of their system and then determine how the components of that model will behave under the circumstances of interest. In fMRI simulations, the cerebrovasculature is naturally the system to model due to its intimate connection with the BOLD signal. Most frequently, it is modelled as a collection of randomly oriented, infinitely long cylinders, where each cylinder represents a blood vessel [19-27], but it is also possible to use a real vascular map obtained from experimental data [28]. Each of the vessels perturbs the static magnetic field in both the intravascular (IV) and extravascular (EV) space. Using these models, the MR signal is typically derived using either Monte Carlo (MC) methods [19-21, 24, 25, 27], analytical equations [9, 29], or deterministic simulations [22, 23, 26, 28]. The MC method stochastically simulates the diffusion of individual protons distributed throughout the cerebrovasculature and calculates the phase accrued throughout each proton's history. Analytical models do not directly model the cerebrovasculature; instead, they attempt to reduce the predicted MR signal to an equation or set of equations that depend on several factors, including signal contributions from IV and EV space. Finally, deterministic simulations discretize both the cerebrovasculature and the time increment over which the system of transverse magnetization evolves. The process of diffusion, which is inherently stochastic, also gets modelled deterministically.

Deterministic simulations appear to provide an attractive alternative for simulating the MR signal due to the potential speed increases over MC simulations and the greater level of control and variability over analytical equations; however, to date, validation of the method has been lacking in the literature, especially when including diffusion. This thesis presents a thorough investigation into the effects of various model parameters on the accuracy of the simulations. Validation is performed on a homogeneous system void of any blood vessels and also using a realistic distribution of blood vessels in a voxel, both with and without diffusion. The thesis breakdown is as follows:

Chapter 2 covers the requisite background material for describing the deterministic simulations: this includes basic MR theory and brain physiology; building from these two topics, the origins of the BOLD signal are described; and finally, other numerical and analytical models of the BOLD signal are described for comparison with the deterministic model. Chapter 3 gives a detailed description of the deterministic model and describes all of the simulations that were run for validating the model. The later chapters include the traditional Results, Discussion, and Conclusion sections.

Chapter 2 Background

2.1 MR Theory

This section covers the basics of MR physics, describing the precession and relaxation of nuclear magnetization in the presence of a static magnetic field. Nuclear magnetic resonance (NMR) is fundamentally a quantum mechanical process but in most applications is adequately characterized using classical mechanics. In this section, a largely classical approach is taken to describe the basics of MR theory, however, unavoidable quantum mechanical concepts are used as well.

2.1.1 Nuclear Spin

For every nucleus with an odd number of nucleons (the total number of protons and neutrons), there exists an intrinsic angular momentum known as the spin angular momentum, $\mathbf{S}$. Since the nucleus is charged and has an angular momentum, it also has a magnetic moment, $\boldsymbol{\mu}$, given by

$$\boldsymbol{\mu} = \gamma \mathbf{S} \tag{2.1}$$

where γ is the gyromagnetic ratio of the nucleus. A list of the gyromagnetic ratios of some commonly imaged nuclei is given in Table 2.1. The spin angular momentum and the magnetic moment can be pictured classically as arising from a charged sphere spinning about an axis through its centre.

Table 2.1: List of the gyromagnetic ratios of commonly imaged nuclear species.

Nucleus	$\frac{\gamma}{2\pi}$ [MHz/T]
^{1}H	42.577
^{13}C	10.705
^{19}F	40.054
^{23}Na	11.262
^{31}P	17.235

2.1.2 Nuclear Spins in a Static Magnetic Field

When nuclear spins are subjected to a static magnetic field, $\mathbf{B_0}$, two things happen: a majority of the spins will tend to align with the field and the spins will precess about the direction of the field. The former process can be described quantum mechanically by considering that the nuclei will preferentially populate the lowest energy state, which in this case is when $\boldsymbol{\mu}$ and $\mathbf{B_0}$ are parallel. The latter process of precession can be described classically by considering the torque acting on a single nucleus due to the static magnetic field. This torque, $\boldsymbol{\tau}$, is equal to the time rate of change of the angular momentum and is also given by

$$\boldsymbol{\tau} = \frac{d\mathbf{S}}{dt} = \boldsymbol{\mu} \times \mathbf{B_0} \tag{2.2}$$

Since $\boldsymbol{\mu}$ and $\mathbf{S}$ are related by Eq.(2.1), multiplying Eq. (2.2) by γ results in the following

$$\frac{d\boldsymbol{\mu}}{dt} = \boldsymbol{\mu} \times \gamma \mathbf{B_0} \tag{2.3}$$

This tells us that the magnetic moment will follow a trajectory that is perpendicular to both the direction it and $\mathbf{B_0}$ point in and its magnitude will remain constant over time. This solution of motion describes precession of $\boldsymbol{\mu}$ about $\mathbf{B_0}$ at a frequency given by

$$\begin{aligned} \omega_0 &= \gamma B_0 \quad \text{in rad} \cdot \text{s}^{-1} \\ f_0 &= \frac{\gamma}{2\pi} B_0 \ \text{in Hz} \end{aligned} \tag{2.4}$$

ω_0 is known as the Larmor frequency, it clearly depends on the nuclear species being studied and it is dependent on the field strength.

When considering a system of nuclei in a volume V, as is the case when imaging an object, the sum of the individual magnetic moments per unit volume gives the net magnetization $\boldsymbol{M}$ of the system:

$$\boldsymbol{M} = \frac{1}{V} \sum_{\text{nuclei in } V} \boldsymbol{\mu_i} \tag{2.5}$$

Due to the linearity of Eq. (2.3), the net magnetization follows the same relation as the individual magnetic moments, that is

$$\frac{d\boldsymbol{M}}{dt} = \boldsymbol{M} \times \gamma \mathbf{B_0}. \tag{2.6}$$

Therefore, the net magnetization also precesses about $\mathbf{B_0}$ at the Larmor frequency.

In comparison to the magnitude of the static magnetic field, the field produced by the net magnetization in the direction of $\mathbf{B_0}$ is negligible and very difficult to measure directly. In order to detect this magnetization, it first gets excited from the longitudinal direction (parallel to $\mathbf{B_0}$) into the transverse plane (perpendicular to $\mathbf{B_0}$) by applying another magnetic field, $\mathbf{B_1}$, for a short duration of time along the transverse direction and rotating at the Larmor frequency. At this stage, the magnetization will precess about $\mathbf{B_0}$ at the Larmor frequency and it can be easily detected by electromagnetic induction.

2.1.3 Relaxation

In addition to precession about $\mathbf{B_0}$, once excited into the transverse plane by the $\mathbf{B_1}$ field, the net magnetization will return to equilibrium along the longitudinal direction via relaxation by two different mechanisms: spin-lattice relaxation causes the longitudinal magnetization, M_z, to regrow until it reaches its equilibrium value M_0; spin-spin relaxation causes the transverse magnetization, M_{xy}, to decay away to zero.

Longitudinal relaxation is caused by the extra energy imparted to the proton spin system[1] by the radiofrequency (RF) excitation being dissipated into the surrounding tissue's molecular lattice (hence the term spin-lattice relaxation). Phenomenologically, longitudinal magnetization regrows exponentially to the equilibrium magnetization with a time constant T_1 and can be described by Eq. (2.7).

$$\frac{dM_z}{dt} = -\frac{M_z - M_0}{T_1}, \tag{2.7}$$

which, for start time t_0, has the solution

$$M_z(t) = M_0\left(1 - e^{-(t-t_0)/T_1}\right) + M_z(t_0)e^{-(t-t_0)/T_1}. \tag{2.8}$$

The decay of the transverse magnetization is the result of dephasing of the individual magnetic moments. This dephasing is caused by the interactions of neighbouring spins that create microscopic inhomogeneities in the static field, which therefore alter the local Larmor frequency of precession. Transverse relaxation can be described phenomenologically by exponential decay with a time constant T_2:

$$\frac{dM_{xy}}{dt} = -\frac{M_{xy}}{T_2}, \tag{2.9}$$

which, for start time t_0, has the solution

$$M_{xy}(t) = M_{xy}(t_0)e^{-(t-t_0)/T_2} \tag{2.10}$$

[1] Hydrogen nucleus or proton will be used instead of the generic term nuclear species since this thesis focuses on hydrogen imaging.

In reality, B_0 is never completely homogeneous due to hardware limitations and variations in tissue susceptibilities. Static field inhomogeneities lead to a distribution of precessional frequencies in the tissue, which in turn leads to quicker dephasing of the transverse magnetization. This can also be described by exponential decay with an *apparent* transverse decay time constant T_2^* given by intrinsic (T_2) and extrinsic (T_2') contributions:

$$\frac{1}{T_2^*} = \frac{1}{T_2} + \frac{1}{T_2'}$$
$$\text{or} \tag{2.11}$$
$$\frac{1}{T_2^*} = R_2^* = R_2 + R_2'$$

where R_2^* is the apparent transverse relaxation rate, R_2 is the irreversible component of the transverse relaxation rate, and R_2' is the reversible component of the transverse relaxation rate[2].

2.1.4 Bloch Equations

By combining Eqs. (2.6), (2.7), and (2.9), the time evolution of the magnetization can be described in what are known as the Bloch equations (represented here in vector form as a single equation):

$$\frac{d\boldsymbol{M}}{dt} = \boldsymbol{M} \times \gamma \mathbf{B} - \frac{M_x \hat{\boldsymbol{x}} + M_y \hat{\boldsymbol{y}}}{T_2} - \frac{M_z - M_0}{T_1} \hat{\boldsymbol{z}}\,, \tag{2.12}$$

where M_x and M_y are the x- and y-components of $\boldsymbol{M}$, respectively. Note that $\mathbf{B_0}$ in Eq. (2.6) is replaced in the equation above by $\mathbf{B}$ since multiple fields can be applied in addition to $\mathbf{B_0}$. Therefore, the Bloch equations describe both the precession of the nuclear magnetization about any arbitrary magnetic field – represented by the cross-product – and the relaxation of the longitudinal and transverse nuclear magnetization—represented by the T_1 and T_2 terms. To simplify the analysis greatly, typically the equations are

[2] It is referred to as the reversible component because it is possible with a spin echo sequence to refocus the dephasing that occurs due to the static field inhomogeneities.

evaluated from a frame of reference rotating at the Larmor frequency, such that the $\mathbf{B_0}$ field disappears.

2.2 Brain Physiology

Neurons are the primary cells of all animals' nervous systems. They are uniquely shaped cells whose role is to transmit and receive electrical signals across the body in order to control the body's functions. A model neuron is illustrated in Figure 2.1. Incoming electrical signals are first received by *dendrites* – thin, branched processes that carry the signal to the cell body. The incoming signals are then processed in the cell body where they will either be propagated or they will die. Neurons also have a single branching *axon* extending outward from the cell body that carries outgoing signals. Finally, at the ends of the axon branches are axon terminals, which contact dendrites or cell bodies of other cells (neurons or otherwise) forming *synapses*. In the brain, the cell bodies and synapses are primarily concentrated in grey matter (GM) but their axons can pass through white matter connecting remote regions of GM and forming complex neural networks.

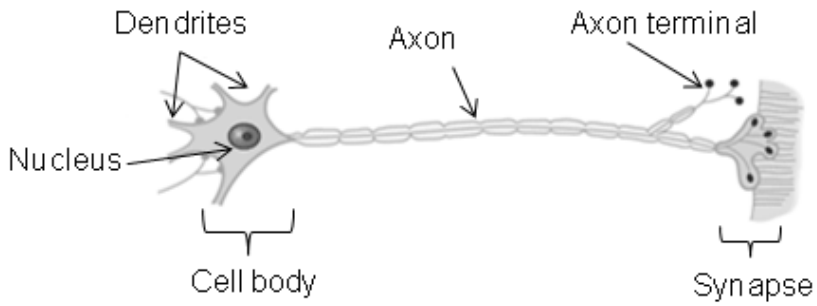

Figure 2.1: Schematic of a neuron containing a cell body that processes incoming signals, multiple dendrites that receive incoming graded potentials, a single axon that transmits action potentials, and axon terminals that transmit the electrical signal. Adapted from [30].

2.2.1 Membrane Potential, Graded Potentials, and Action Potentials

In all neurons, a potential difference exists across the cell membrane; it is produced by an unequal distribution of ions in the intra- and extra-cellular spaces. The principal ions involved in this are Na^+, K^+, Cl^-, and Ca^{2+}. In the basal state, the membrane potential is approximately -70 mV (where the inside of the cell is at the more negative potential) and

it is influenced by the concentration gradient of ions across the membrane and the permeability of the membrane to the ions.

When a neuron receives a signal from another neuron, the membrane potential is the physiological property that gets altered. Ion channels across the membrane open and close in a coordinated fashion allowing ions to flow in or out of the cell depending on the concentration and electrical gradients of the ions. The input signals arrive in the dendrites or cell body and they can be depolarizing (potential difference becomes less negative) or hyperpolarizing (potential difference becomes more negative). The amplitudes of such polarizations, known as *graded potentials*, are dependent on the strength of the triggering event and they diminish with distance. When a graded potential is produced, a wave of polarization travels through the cell and reaches the trigger zone near the origin of the axon. At the trigger zone, if a polarization threshold is reached (approximately -55 mV), an *action potential* (described in the next paragraph) is produced in the cell; otherwise, the graded potential dies away. Graded potentials are additive, therefore the cell can integrate multiple inputs simultaneously.

Signal transmission from a neuron starts at the trigger zone – where an action potential is first produced – and travels down the axon. Action potentials, also known as spikes, are rapid depolarizing events of approximately 100 mV amplitude that differ from graded potentials in two major ways: action potentials are identical to each other for each neuron and they do not diminish in strength as they travel through the cell. Referring to Figure 2.2, the typical steps in an action potential are [31]:

1. A depolarizing stimulus reaches the trigger zone.
2. The membrane potential depolarizes to threshold, voltage-gated Na^+ channels open causing Na^+ ions to enter the cell. Voltage-gated K^+ channels begin to open slowly.
3. Rapid Na^+ entry depolarizes the cell.
4. Na^+ channels close and slower K^+ channels open.
5. K^+ *exits* the cell.
6. K^+ channels remain open and K^+ continues to leave the cell leading to a hyperpolarization.

7. As K^+ channels close, some K^+ leaks back into the cell.
8. The region returns to its resting ion permeability and membrane potential.

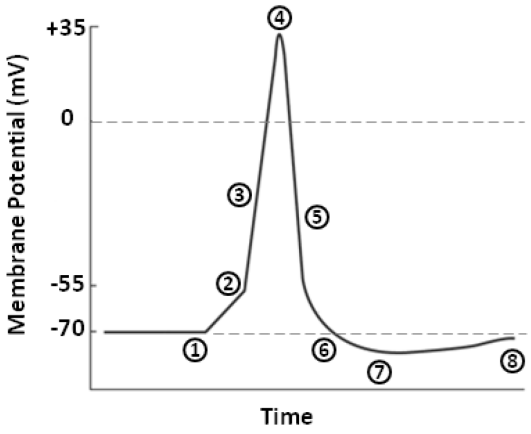

Figure 2.2: The evolution of an action potential over time. The steps are described in the text. Adapted from [30].

The onset of the action potential at the trigger zone raises the membrane potential where the axon originates and initiates a cascade of action potentials that travels down the axon towards the axon terminal. Unlike graded potentials, the magnitude and form of an action potential is the same regardless of the strength or duration of the stimulus. To encode the stimulus strength and duration, the spiking *frequency* is modulated in proportion to the two, i.e., a stronger or longer duration input will produce a train of more closely packed action potentials.

When the action potential arrives at the axon terminal, the signal can either be transmitted directly across the synapse at an *electrical synapse* or it can be transmitted to the next cell using neurotransmitters at a *chemical synapse*. In a chemical synapse, voltage-gated Ca^{2+} ion channels open up when the action potential arrives, creating an influx of Ca^{2+} ions. The influx of Ca^{2+} triggers the release of neurotransmitters into the synaptic cleft. The neurotransmitters then bind to receptors on the post-synaptic cell, where a response is initiated.

2.2.2 Neurovascular Coupling

From a thermodynamic perspective, neural signalling is an energetically downhill process [32] since the system is maintained far from equilibrium and allowed to approach closer to equilibrium during signalling. Returning the neuronal ionic gradients to their basal levels requires energy metabolism, this is fueled by adenosine triphosphate (ATP) consumption and the ATP is replenished by oxidative metabolism of glucose.

The brain does not have large reserves of glucose or oxygen however, requiring the two to be constantly delivered to the brain through the blood supply. Glucose is dissolved in plasma and it diffuses down its gradient from blood into tissue when it enters the capillary bed. Oxygen, on the other hand, has very low solubility in plasma; to compensate, the vast majority of O_2 is transported bound to hemoglobin in red blood cells. Although the amount of O_2 dissolved in plasma is negligible compared to the amount bound to hemoglobin, it is the source of O_2 for tissue. Once in the capillary bed, the O_2 dissolved in plasma diffuses out of the vessel into the tissue. This diffusion is driven by the partial pressure of O_2 gradient between plasma and tissue. The O_2 molecules diffusing out of plasma are rapidly replenished by hemoglobin-bound O_2, allowing for a substantial amount of O_2 transfer from blood to tissue. It has been found using positron emission tomography (PET) studies that the oxygen extraction fraction in humans is approximately 40% in the resting state and is fairly constant across the healthy brain [33]. With the use of a variety of imaging techniques, it has been well established that cerebral blood flow (CBF), the cerebral metabolic rate of glucose (CMRGlc), and the cerebral metabolic rate of oxygen ($CMRO_2$) all increase in activated regions of the healthy brain [34, 35].

Given the neuronal demands for glucose and O_2, there must be a mechanism for affecting the vasculature when neural activity is increased. In addition to neuronal cells, the brain is populated by a large number of support cells called *glial* cells. These cells account for almost half of the cells in the brain and were originally thought to serve as a structural scaffold [36]. *Astrocytes* are a type of glial cell that have numerous processes in contact with both neuronal synapses and blood vessels and may transfer nutrients between the two [31]. There is now significant evidence that astrocytes play a pivotal role

in coupling the control of cerebral blood flow (CBF) with neuronal activity [37]. Upon neuronal activation, neurotransmitters can bind to receptors on the astrocyte leading to ion transfers within the astrocyte and at its processes near arterioles. Upon interaction with the ions, the smooth muscle surrounding the arteriole can relax or contract, therefore controlling the CBF by controlling the arteriolar diameter. This relationship between neuronal activity, energy metabolism, and CBF is known as neurovascular coupling and it provides the physiological foundation for most functional neuroimaging.

2.3 Origins of the BOLD Signal

So far, much of the discussion has focussed on the basis of MRI and the physiological changes occurring during neural signalling, but how can the former be made sensitive to the latter? For this to be clear, it is important that the physiological properties and their relationships be formally defined.

2.3.1 CBF, CBV, and $CMRO_2$

CBF is defined as the rate of delivery of arterial blood to the capillary beds of a particular mass of tissue. Its units are mL blood per 100 g of tissue per min but since in imaging it is easier to determine the tissue volume rather than mass, CBF is often given in units of mL blood per 100 mL tissue per min. CBF and $CMRO_2$ are fundamentally linked through the Fick Principle expressing the conservation of mass:

$$\mathrm{CMRO_2} = \mathrm{OEF} \cdot \mathrm{CBF} \cdot [\mathrm{O_2}]_a, \tag{2.13}$$

where OEF is the oxygen extraction fraction and $[\mathrm{O_2}]_a$ is the arterial concentration of O_2. The product $\mathrm{CBF} \cdot [\mathrm{O_2}]_a$ gives the rate of O_2 delivery to the capillary bed; therefore, $CMRO_2$ represents the rate of O_2 extraction from the capillary bed. The units of $CMRO_2$ are moles of O_2 per 100 g (or 100 mL) per min.

The cerebral blood volume (CBV) is the fraction of tissue volume occupied by blood vessels and it is a dimensionless quantity (mL blood per mL tissue). The typical CBV in GM is approximately 4% [38]. CBV can be further broken down into the different vascular components: arterial (CBV_a), capillary (CBV_c), and venous (CBV_v), where CBV_a has been estimated to be about 20% and CBV_c and CBV_v being in the range of 30% – 50% (such that the total of the three adds up to 100%) [39-41].

The flow of blood through vessels is chiefly dependent on two things: the pressure difference between arterial and venous blood and the blood's resistance to flow, such that

$$\mathrm{CBF} = \frac{\Delta P}{\mathrm{CVR}}, \tag{2.14}$$

where ΔP is the pressure difference and CVR is the cerebrovascular resistance. For purely laminar flow, CVR is given by the Hagen-Poiseuille law, which states that

$$\mathrm{CVR} \propto 1/r^4 \tag{2.15}$$

where r is the vessel radius [42]. Combining Eqs. (2.14) and (2.15) and noting that CBV is proportional to r^2, it can be shown that CBV and CBF have a power-law relationship:

$$\frac{\mathrm{CBV}}{\mathrm{CBV_0}} = \left(\frac{\mathrm{CBF}}{\mathrm{CBF_0}}\right)^{\alpha}. \tag{2.16}$$

The exponent α is used because in reality the flow is not perfectly laminar and also because vessel dilations and contractions are not constant along the entire vascular tree[3]. As a result of all these factors, determining α from first principles is not straightforward, however it has been determined empirically from PET studies with monkeys to be 0.38 [43].

2.3.2 Modelling the BOLD Signal

As described in Section 2.2.2, most O_2 is transported by blood and bound to hemoglobin. More precisely, hemoglobin is a large protein complex, which can carry up to four O_2 molecules. It consists of four polypeptide chains, each one with a prosthetic heme group bound to it [44]. At the centre of each heme group is an iron ion in the ferrous oxidation state (Fe^{2+}) that is capable of binding O_2. The binding of O_2 to iron substantially rearranges the electrons in the ion leading to a conformational change of the hemoglobin molecule. This electronic rearrangement is paralleled by a change in the volume susceptibility of hemoglobin, switching from being paramagnetic in the deoxygenated state to diamagnetic in the oxygenated state [45] (with a similar volume susceptibility as tissue [46]). Thus, depending on the blood oxygenation level, the susceptibility of blood will be different than the surrounding tissue's. Where susceptibilities differ, offsets in the

[3] When the arteriole diameter increases, a stronger driving pressure on the downstream vessels causes the capillaries and venules to passively dilate.

B_0 field arise and lead to quicker dephasing of the transverse magnetization, as described in Section 2.1.3.

Intuitively, one might imagine that if $CMRO_2$ and CBF both increased to meet the increased metabolic demands during neural signalling, that either the venous concentration of dHb ($[dHb]_v$) would remain constant or it would increase due to increased O_2 consumption. If $[dHb]_v$ remained constant, there would be no change in R_2^* and therefore no BOLD effect. If $[dHb]_v$ increased, R_2^* would increase and therefore the signal would decrease. Contrary to intuition, there is a significantly larger increase in CBF than in $CMRO_2$ resulting in a decrease in $[dHb]_v$, a decrease in R_2^*, and, therefore, an *increase* in the measured BOLD signal [3-5].

These changes in R_2^* can be modelled by considering R_2^* to be composed of a component that includes all the effects due to dHb ($R_{2_{\mathrm{dHb}}}^*$) and another component that accounts for all other effects ($R_{2_{\mathrm{other}}}^*$) [11]:

$$R_2^* = R_{2_{\mathrm{dHb}}}^* + R_{2_{\mathrm{other}}}^*. \tag{2.17}$$

It was found using Monte Carlo simulations that $R_{2_{\mathrm{dHb}}}^*$ was dependent on CBV and $[dHb]_v$ [35]:

$$R_{2_{\mathrm{dHb}}}^* = k \cdot \mathrm{CBV} \cdot [\mathrm{dHb}]_v^{\beta}, \tag{2.18}$$

where k is a field strength and sample-specific constant of proportionality and β is a factor that accounts for the IV and EV contributions to the BOLD signal. β is field strength-dependent and was determined by Monte Carlo simulations at 1.5 T to be 1.5 [20] and more recently, studies at 3 T have empirically determined it is 1.3 [47]. If the "other" sources contributing to R_2^* remain constant under activation, the change in R_2^* away from baseline can be expressed as

$$\Delta R_2^* = k\left(\mathrm{CBV} \cdot [\mathrm{dHb}]_v^{\beta} - \mathrm{CBV}_0 \cdot [\mathrm{dHb}]_{v,0}^{\beta}\right), \tag{2.19}$$

where the subscript '0' represents the value at baseline.

This model of transverse relaxation can be incorporated into the basic signal equation that applies during gradient echo imaging:

$$S = Ae^{-\mathrm{TE}\cdot R_2^*}, \tag{2.20}$$

where A is a catch-all constant that depends on spin density, flip angle, field strength, receiver sensitivity, etc. and TE is the echo time. Under neuronal activation, small signal changes occur and by taking up to the first order term in the Taylor expansion of Eq. (2.20), the relative signal change can be approximated as

$$\begin{aligned}\frac{\Delta S}{S} &\cong -\mathrm{TE}\cdot\Delta R_2^* \\ &= k\cdot\mathrm{TE}\left(\mathrm{CBV}_0\cdot[\mathrm{dHb}]_{v,0}^{\beta} - \mathrm{CBV}\cdot[dHb]_v^{\beta}\right) \\ &= k\cdot\mathrm{TE}\cdot\mathrm{CBV}_0\cdot[\mathrm{dHb}]_{v,0}^{\beta}\left(1-\frac{\mathrm{CBV}}{\mathrm{CBV}_0}\left(\frac{[\mathrm{dHb}]_v}{[\mathrm{dHb}]_{v,0}}\right)^{\beta}\right) \\ &= M\left(1-\frac{\mathrm{CBV}}{\mathrm{CBV}_0}\left(\frac{[\mathrm{dHb}]_v}{[\mathrm{dHb}]_{v,0}}\right)^{\beta}\right).\end{aligned} \tag{2.21}$$

The factor M out front of Eq. (2.21) is known as the BOLD calibration constant.

$$M \equiv k\cdot\mathrm{TE}\cdot\mathrm{CBV}_0\cdot[\mathrm{dHb}]_{v,0}^{\beta} \tag{2.22}$$

Under the assumption that all O_2 in blood is bound to hemoglobin with four O_2 molecules per molecule of hemoglobin, $[\mathrm{dHb}]_v$ can be approximated as $[\mathrm{dHb}]_v \approx \mathrm{OEF}\cdot[\mathrm{O_2}]_a/4$. Combining this with the Fick Principle in Eq. (2.13) and the fact that $[O_2]_a$ is essentially a constant, the ratio of [dHb] in the activated state to baseline is given by

$$\frac{[\mathrm{dHb}]_v}{[\mathrm{dHb}]_{v,0}} = \frac{\mathrm{CMRO_2}}{\mathrm{CMRO_{2,0}}}\frac{\mathrm{CBF_0}}{\mathrm{CBF}}. \tag{2.23}$$

Combining this last result with Eq. (2.21) gives the biophysical model of the BOLD equation:

$$\frac{\Delta S}{S} = M\left(1-\frac{\mathrm{CBV}}{\mathrm{CBV}_0}\left(\frac{\mathrm{CBF}}{\mathrm{CBF_0}}\right)^{-\beta}\left(\frac{\mathrm{CMRO_2}}{\mathrm{CMRO_{2,0}}}\right)^{\beta}\right). \tag{2.24}$$

Finally, this Eq. (2.24) can be further simplified using the power-law relationship between CBF and CBV in Eq. (2.16):

$$\frac{\Delta S}{S} = M\left(1 - \left(\frac{\mathrm{CBF}}{\mathrm{CBF}_0}\right)^{\alpha-\beta}\left(\frac{\mathrm{CMRO}_2}{\mathrm{CMRO}_{2,0}}\right)^{\beta}\right). \tag{2.25}$$

It was mentioned above that α was determined by PET imaging to be 0.38 [43], however, this value was measured for changes in CBV and CBF throughout the entire microvascular tree (arterioles, capillaries, and venules) but since BOLD imaging depends on the concentration of dHb, this makes it much more sensitive to the changes occurring in the venules and capillaries (and in the arterioles to a much lesser extent since arterial blood is almost completely oxygenated). As a result of this, α was measured again using MR methods that are sensitive to the deoxygenated CBV (dCBV) and a new value of approximately 0.2 was found [48, 49].

By reordering the terms in Eqs. (2.24) or (2.25), it is possible to express the relative change in $CMRO_2$ in terms of the relative BOLD signal changes, CBF and/or CBV changes, and the calibration constant *M*. Several techniques have been proposed for measuring the calibration constant and this was the motivating factor for investigating computer simulations of BOLD fMRI. By knowing the physiological ground truth defined by the simulation parameters, it would be possible to perform an absolute comparison of the different calibration techniques under a variety of circumstances. Calibration techniques have employed hypercapnic and/or hyperoxic gas challenges to modulate $[\mathrm{dHb}]_v$ or CBF without affecting $CMRO_2$ [11, 35, 50, 51]. This can be both cumbersome for the technicians/researchers and uncomfortable for the subjects but a recently proposed technique removes the necessity of gas challenges by using a baseline measurement of R_2' to estimate *M* [52]. It was specifically this latter technique that motivated the use of the simulations, therefore measurement of R_2' is often used throughout this thesis as a metric for comparison.

2.4 Numerical Simulations of BOLD fMRI

Since the early days of BOLD imaging, researchers have been using simulations to probe the origins of the effect [19, 20] and many of the advances in fMRI have been made because of the results obtained from simulations. For numerically modelling the BOLD signal, there have been three major methods employed: Monte Carlo (MC) simulations, analytical models, and deterministic simulations. Analytical models are unique from the other two techniques in that they do not calculate the history of the transverse magnetization, instead they can directly compute the BOLD signal at any time from a pre-determined functional form of the signal. MC and deterministic simulations, on the other hand, compute the transverse magnetization's history throughout time.

MC methods and some analytical models of the BOLD signal are briefly presented here while deterministic simulations are described in more detail in Chapter 3. But first, molecular diffusion is described since it is a fundamental factor contributing to the decay of transverse magnetization. By the process of diffusion through an inhomogeneous B_0 field, protons accrue irreversible phase over time that results in additional loss of signal.

2.4.1 Molecular Diffusion Theory

The original theory of molecular diffusion was developed by Fick in 1855 and was used to describe the flux of molecules ($\mathbf{J}$) in a molecular concentration gradient (∇C); Fick's first law of diffusion is [53]

$$\mathbf{J} = -D\nabla C, \tag{2.26}$$

where the diffusion coefficient, D, is a constant of proportionality. By combining Eq. (2.26) with the conservation of mass law,

$$\frac{\partial C}{\partial t} = \nabla \cdot \mathbf{J}, \tag{2.27}$$

and assuming D is constant, we get Fick's second law of diffusion:

$$\frac{\partial C}{\partial t} = -D\nabla^2 C. \tag{2.28}$$

Eq. (2.28) has many solutions depending on the initial conditions and the boundary conditions. For particles satisfying the boundary condition $C(|\mathbf{r}| \to \infty,\ t) = 0$ and the initial condition $C(\mathbf{r}, t = 0) = \delta(\mathbf{r} - \mathbf{r_0})$, known as free self-diffusion since there are no boundaries and no concentration gradient driving the diffusion, the solution for the evolution of the concentration over time and space in three dimensions is

$$C(\mathbf{r}, t) = \frac{1}{(4Dt)^{3/2}} \exp\left[-\frac{(\mathbf{r} - \mathbf{r_0}) \cdot (\mathbf{r} - \mathbf{r_0})}{4Dt}\right]. \tag{2.29}$$

From this expression, one can see that the distribution of the concentration due to self-diffusion is a normalized Gaussian function with a variance $\sigma^2 = 2Dt$, meaning its width increases in time.

When interested in the movement of individual molecules, it was Einstein who made the connection between the concentration distribution and the *probability* of a molecule diffusing a particular distance [54]. The probability P of a molecule starting at position $\mathbf{r_0}$ and moving to an infinitesimal volume dV located at $\mathbf{r}$ obeys the same rules as the concentration distribution above and is therefore given by

$$P(\mathbf{r}|\mathbf{r_0}, t)dV = \frac{dV}{(4Dt)^{3/2}} \exp\left[-\frac{(\mathbf{r} - \mathbf{r_0}) \cdot (\mathbf{r} - \mathbf{r_0})}{4Dt}\right]. \tag{2.30}$$

It can be seen that the probability only depends on the net displacement, $\mathbf{R} = \mathbf{r} - \mathbf{r_0}$, of the molecule, so it is convenient to define

$$P(\mathbf{R}, t) \equiv P(\mathbf{r}|\mathbf{r_0}, t). \tag{2.31}$$

One can also determine the probability distribution along a single dimension by rewriting Eq. (2.30) in Cartesian coordinates and by integrating out two of the dimensions. The probability, therefore, of self-diffusion a distance X along the x-axis, is

$$P(X,t)dx = \frac{dx}{(4Dt)^{1/2}} \exp\left[-\frac{X^2}{4Dt}\right]. \tag{2.32}$$

Given the probability for a molecule's displacement, it is possible to determine the different moments of the distribution. Clearly, the first moment is zero, which represents the fact that the molecule is equally likely to diffuse in all directions since this is free self-diffusion. However, the second moment, the mean square diffusion distance, is

$$\begin{aligned} \langle X^2 \rangle &= 2Dt \quad \text{in 1D} \\ \langle \mathbf{R^2} \rangle &= 6Dt \quad \text{in 3D.} \end{aligned} \tag{2.33}$$

This dependence of the mean square diffusion distance on *D* suggests a method for directly probing the diffusivity of a medium and is in fact the basis for diffusion MRI [53]. In vivo, diffusion is restricted, so the measured diffusion coefficient is referred to as the *apparent* diffusion coefficient (ADC). Table 2.2 gives a list of some typical ADCs of different brain tissues measured by diffusion MRI.

Table 2.2: Apparent diffusion coefficient (ADC) values for brain tissues. Values from [55].

Tissue Type	ADC (mm^2/ms)
Cerebrospinal fluid	2.94 ± 0.05
Grey matter	0.76 ± 0.03
White matter	
corpus callosum	0.22 ± 0.22
axial fibres	1.07 ± 0.06
transverse fibres	0.64 ± 0.05

The theory above described the probability of a *single* molecule's diffusion; when considering an ensemble of molecules, the total probability, $\Psi(\mathbf{r}, t)$, of finding a molecule with position $\mathbf{r}$ after time interval *t*, is given by the integral of each individual particle's probability of self-diffusion weighted by the initial distribution of particles, $\rho(\mathbf{r})$ [56]:

$$\Psi(\mathbf{r},t) = \int \rho(\mathbf{r}')P(\mathbf{r}|\mathbf{r}',t)d\mathbf{r}'. \tag{2.34}$$

Using $\rho(\mathbf{r}) = \delta(\mathbf{r} - \mathbf{r_0})$ like above, $\Psi(\mathbf{r},t)$ reduces to $P(\mathbf{r}|\mathbf{r_0},t)$. Therefore, the ensemble moments are exactly the same as the individual molecules' moments.

The Bloch-Torrey Equation

The phenomenological Bloch equations, described in Section 2.1.4, can be extended to include the effects of diffusion. This modification, suggested by Torrey, adds a diffusion term to the description of the transverse magnetization after a 90° excitation and is known as the Bloch-Torrey equation [57]:

$$\frac{\partial M_{xy}}{\partial t} = -i(\omega_0 + \gamma \mathbf{G}\cdot\mathbf{r})M_{xy} - \frac{M_{xy}}{T_2} + D\nabla^2 M_{xy} \tag{2.35}$$

In this form, Eq. (2.35) looks slightly different from the Bloch equations presented in Eq. (2.12): the first term in parentheses represents the precession of M_{xy} in the static field B_0 as well due to any additional gradients (**G**) in the z-component of the magnetic field experienced by a spin at position **r**; the second term is the T_2 decay; and the third term describes the diffusion.

2.4.2 Monte Carlo Simulations

MC simulations are the gold standard for MRI simulations because they provide low-level control of the underlying physics including the temporal and spatial dynamics of the system. The physics for modelling the BOLD effect is simple: protons diffusing through an inhomogeneous magnetic field acquire phase differences relative to each other leading to a reduced macroscopic transverse magnetization and signal.

The model for producing the field perturbations varies from study to study but the vast majority of studies use an infinite cylinder model [19-27]. In this model, blood vessels are represented as infinite cylinders of uniform volume susceptibility, which is dependent on the blood oxygen saturation (S_bO_2) and the hematocrit (Hct) – the fractional volume of blood occupied by hemoglobin. Assuming that the volume susceptibility of

fully oxygenated blood is the same as tissue's, then the susceptibility difference between the cylinder and the surrounding medium (tissue) is equal to $\Delta\chi_{do}\cdot\mathrm{Hct}\cdot(1-\mathrm{S}_b\mathrm{O}_2)$, where $\Delta\chi_{do}$ is the susceptibility difference between fully deoxygenated blood and fully oxygenated blood. Based on the orientation of the blood vessel relative to B_0 and the susceptibility difference between the vessel and the surrounding medium (tissue), the field offset, ΔB_z, in the z-direction is given by [19]

$$\Delta B_z = \Delta B_z' \times \begin{cases} \left(\frac{a}{r}\right)^2 \sin^2(\theta)\cos(2\phi) & \text{outside cylinder} \\ \cos^2(\theta) - 1/3 & \text{inside cylinder} \end{cases} \qquad (2.36)$$

$$\text{where} \quad \Delta B_z' \equiv 2\pi\Delta\chi_{do}\mathrm{Hct}(1-\mathrm{S}_b\mathrm{O}_2)B_0.$$

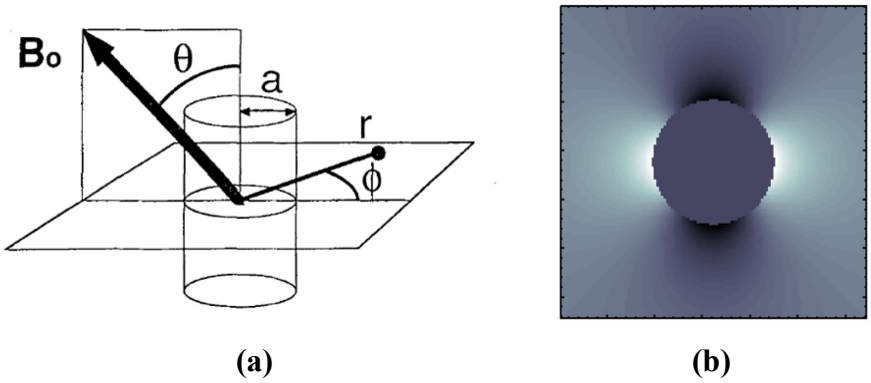

(a) **(b)**

Figure 2.3: Geometry used to describe the field offsets produced by an infinite cylinder susceptibility variation (a) (adapted from [22]). Field offset produced by a cylinder oriented perpendicularly to the B_0 field (b), where grey to black is increasingly negative and grey to white is increasingly positive.

Referring to Figure 2.3a, the angle between the cylinder and B_0 is θ, the radius of the cylinder is a, and the perpendicular distance from the cylinder axis to the point of interest is r. ϕ is the angle between the vector from the cylinder axis to the point of interest and the component of B_0 on the plane perpendicular to the cylinder. A characteristic dipole-like field offset is produced by the cylinder (see Figure 2.3b). Due to

the property of superposition, the net field offset at a given point is the sum of the field offsets at that point from all vessels.

The typical steps of a 3D MC simulation are briefly summarized here [21, 24, 58]:

1. On the order of 10^4 protons are randomly placed throughout a voxel filled with homogeneously and randomly oriented blood vessels (cylinders) occupying a fractional volume CBV. Protons can be seeded in both the EV and IV space, however, vessels are typically considered impenetrable. The magnetic moments of all the protons are initially coherent and of unit magnitude.

2. In short time steps ($\delta t \sim 0.2$ ms) the position of each proton is displaced in the *x*-, *y*-, and *z*-directions. The diffusion distance is randomly sampled in each direction from independent, 1D, zero-mean Gaussian distributions with $\sigma^2 = 2D\delta t$ (as in Eq. (2.32)).

3. At each step in the proton's diffusion, the net field offset is calculated using Eq. (2.36) for each vessel. The phase accumulated by the *n*-th proton during each step is given by

$$\Delta\phi_n(t) = \gamma \Delta B_z \delta t. \tag{2.37}$$

4. By expressing the transverse component of each proton's magnetic moment as a rotation in the complex plane ($e^{-i\Delta\phi_n}$), the total signal at each step, $S(t)$, is computed by summing over all N protons' moments:

$$S(t) = \frac{1}{N}\sum_{n=1}^{N} e^{-i\phi_n(t)}. \tag{2.38}$$

5. Steps 1-4 are repeated up to the echo time (TE).

6. In the case of a spin echo (SE) sequence, the sign of the phase is flipped for each proton after the 180° excitation step at TE/2.

Note that in this model, the magnitudes of the individual protons' magnetic moments remain constant (i.e. T_2 decay is ignored), the attenuation is due solely to the susceptibility-induced dephasing.

2.4.3 Analytical Models of the BOLD Signal

The results from the array of MC simulations performed have led to the development of different analytical models of the BOLD signal and they have also been helpful in validating newly proposed models. This is exemplified in a recent model of the BOLD signal equation by Griffeth and Buxton [9] in which the signal is composed of separate contributions from IV and EV compartments and the IV component is further broken down into arterial, capillary, and venous contributions. Empirically derived equations for the EV transverse relaxation rates were taken from the MC results of Ogawa, et al. [19] and empirically derived equations for the IV transverse relaxation rates were taken from experimental measurements [59].

This model and others like it can oversimplify the signal behaviour by, for example, considering only the signal magnitude or assuming mono-exponential decay for each component. By tackling the problem from a more theoretical approach, it can be possible to reproduce more of the intricacies of the signal behaviour.

The Yablonskiy & Haacke Model of NMR Signal Behaviour

By considering only the attenuation due to sources of susceptibility variation, like in the MC simulations, Yablonskiy and Haacke undertook a rigorous theoretical study of the NMR signal [60]. This seminal work explored the theoretical NMR signal behaviour in the presence of tissue inhomogeneities, including blood vessels. Using a statistical approach, they were able to derive analytical solutions for R_2' resulting from a variety of sources/geometries of susceptibility perturbations occupying an otherwise homogeneous volume of tissue. All analysis was performed where the NMR signal was in the static dephasing regime (SDR). This is where magnetic moment dephasing due to local differences in nuclear frequencies is much faster than the time it takes for diffusion to average out the phases of the different nuclei [60]. This regime can be formally defined by

$$\delta\omega \cdot \tau_D \gg 1, \tag{2.39}$$

where the characteristic frequency, $\delta\omega$, is the frequency offset resulting from the magnetic field at the "equator" of the field-creating particle[4], i.e., at the surface of the cylinder where $r = a$ and $\phi = 0°$ in Figure 2.3. The diffusive correlation time, τ_D, is the approximate time a water molecule would take to diffuse past the field perturber:

$$\tau_D = \frac{a^2}{D}. \tag{2.40}$$

In the SDR, spins are subjected to a constant frequency offset determined by Eq. (2.36). By assuming that the number of cylinders was $\gg 1$ and by averaging over all possible cylinder orientations and then averaging over the voxel volume (assuming the volume of the cylinders was negligible), Yablonskiy and Haacke derived the following signal equation:

$$S(t) = k(1 - \mathrm{dCBV})\cdot\exp\left[-\mathrm{dCBV}\cdot\overline{f_c}(\delta\omega\cdot t)\right], \tag{2.41}$$

In Eq. (2.41), k a catch-all factor,

$$\overline{f_c}(x) = \frac{1}{3}\int_0^1 du\cdot(2+u)\cdot\sqrt{1-u}\cdot\frac{1-J_0\left(\frac{3}{2}x\cdot u\right)}{u^2}, \tag{2.42}$$

and the characteristic frequency is given by

$$\delta\omega = \frac{4}{3}\gamma\pi\Delta\chi_{do}\mathrm{Hct}(1-\mathrm{S}_b\mathrm{O}_2)B_0. \tag{2.43}$$

In Eq. (2.42), J_0 is the zeroth order Bessel function.

Asymptotic and numerical calculations suggested two separate behaviours for Eq. (2.41) under short and long time scales:

$$S(t) = \begin{cases} k(1-\mathrm{dCBV})\cdot\exp[-0.3\cdot\mathrm{dCBV}\cdot(\delta\omega\cdot t)^2], & \delta\omega\cdot t < 1.5 \\ k(1-\mathrm{dCBV})\cdot\exp[-R_2'\cdot|t-1/\delta\omega|], & \delta\omega\cdot t > 1.5 \end{cases} \tag{2.44}$$

[4] The term "particle" is used here because the theory was originally developed for sources of inhomogeneity that were spherical particles.

where

$$R_2' = \mathrm{dCBV} \cdot \gamma \frac{4}{3} \pi \Delta \chi_{do} \mathrm{Hct}(1 - \mathrm{S}_b\mathrm{O}_2) B_0. \tag{2.45}$$

In a SE sequence, the long time scale signal can be broken down into three time domains: (A) the free induction decay (FID) prior to the 180° RF pulse, (B) the rephasing between the 180° and the SE, and (C) the resumed FID after the SE. This is illustrated in Figure 2.4 and is mathematically described by

$$S(t) = \begin{cases} S(0)e^{\mathrm{dCBV}}e^{-R_2' \cdot t} & \text{(A) for } 1.5t_c < t < \dfrac{TE}{2} \\ S'(0)e^{\mathrm{dCBV}}e^{-R_2' \cdot (TE-t)} & \text{(B) for } \dfrac{TE}{2} < t < TE - 1.5t_c \\ S'(0)e^{\mathrm{dCBV}}e^{-R_2' \cdot (t-TE)} & \text{(C) for } t > TE + 1.5t_c \end{cases} \tag{2.46}$$

where $t_c = 1/\delta\omega$ is the characteristic time and $S(0)$ and $S'(0)$ both represent the initial signal, however, the prime is included to account for imperfect RF refocusing [23]. In simulations, RF refocusing is typically assumed to be perfect so $S(0) = S'(0)$. Intrinsic T_2 decay can be accounted for by simply multiplying Eqs. (2.41), (2.44), and (2.46) by e^{-t/T_2}.

Looking at Eq. (2.46), it is evident that both dCBV and R_2' can be determined by fitting a spin echo time series in either the (A) and (B) time domains (i.e. about the refocusing pulse) or the (B) and (C) time domains (i.e. about the SE). If in each time domain the log of the signal is linearly fit by an equation of the form $m_\dagger t + b_\dagger$, where † is a place holder for A, B, or C, then R_2' is given by

$$R_2' = \begin{cases} \dfrac{m_\mathrm{B} - m_\mathrm{A}}{2} & \text{if domains (A) \& (B) are fit} \\ \dfrac{m_\mathrm{B} - m_\mathrm{C}}{2} & \text{if domains (B) \& (C) are fit} \end{cases} \tag{2.47}$$

and dCBV is given by

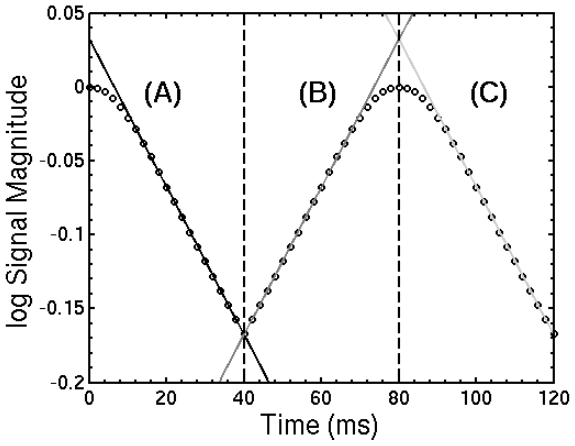

Figure 2.4: Plot of the natural logarithm of the analytical SE signal (open circles) with linear fits included for the long time scale in the three time domains (A), (B), and (C).

$$\text{dCBV} = \begin{cases} (m_{\text{A}} \cdot \text{TE} + b_{\text{A}}) - \ln\big(S(t=0)\big) & \text{if domain (A) is fit} \\ [(m_{\text{B}} + m_{\text{C}}) \cdot \text{TE} + (b_{\text{B}} + b_{\text{C}})] - \ln\big(S(t=\text{TE})\big) & \text{if domains (B) \& (C) are fit.} \end{cases} \tag{2.48}$$

These results hold regardless of whether or not T_2 decay is present.

This theory has been validated in a phantom study using fishing line immersed in distilled water doped with $NiSO_4$•$6H_2O$ and NaC1 and the measured signals matched very closely with theory [61]. Given this agreement between theory and experiment, it should be possible to use this model to validate simulations using cylindrical field perturbers and conversely, to use simulations to test the predictions made by the theory.

Chapter 3 Methods

3.1 3D Model for Deterministic Simulation of M_{xy}

The model of deterministic simulation of M_{xy} investigated in this thesis was originally developed by Bandettini and Wong [22] in two-dimensions (2D) and was later extended to 3D by Klassen and Menon [23]. In 3D, just like in MC simulations, cylinders were homogeneously distributed with random orientations throughout a voxel of tissue. Each vessel was defined through the following steps:

1. The cylinder's azimuth[5], ϕ, was randomly assigned from a uniform distribution ranging from 0 to 2π.

2. The polar angle, θ, was assigned from a $\sin(\theta)/2$ distribution. This was implemented by setting θ equal to $\cos^{-1}(2u-1)$, where u was randomly selected from a uniform distribution ranging from 0 to 1.

3. The position of the cylinder was determined by randomly selecting a single point within the voxel through which the cylinder's central axis would pass. This point

[5]This azimuthal angle ϕ is not the same as the ϕ in Eq. (2.36). Incidentally, the polar angle θ is the same as the one in Eq. (2.36) because B_0 points along the z-direction by convention.

was selected from a uniform distribution ranging from -W/2 to +W/2 for each dimension, where W was the voxel width.

4. In this thesis, cylinder diameters were assigned from a realistic distribution of microvascular diameters obtained by confocal laser microscopy of Indian ink injected human cerebral cortex [41]. In this study, the frequency of one over the square root of the vessel diameters was found to follow an approximately Gaussian probability distribution with mean μ = 0.38 μm$^{-1/2}$ and standard deviation σ = 0.07 μm$^{-1/2}$. The cut-off points for the distribution were 0.1 μm$^{-1/2}$ and 0.6 μm$^{-1/2}$, corresponding to a maximum diameter of 100 μm and minimum diameter of 2.78 μm. The distributions are shown in Figure 3.1.

5. Steps 1-4 were repeated until the desired fractional dCBV was reached. All of this was performed on a voxel with 0.5 cm of padding on all faces (i.e. $W' = W + 1.0$ cm) in order to (a) ensure that the effect of distant vessels could still be felt within the voxel and (b) reduce the scarcity of vessels at the edges of the voxel [21].

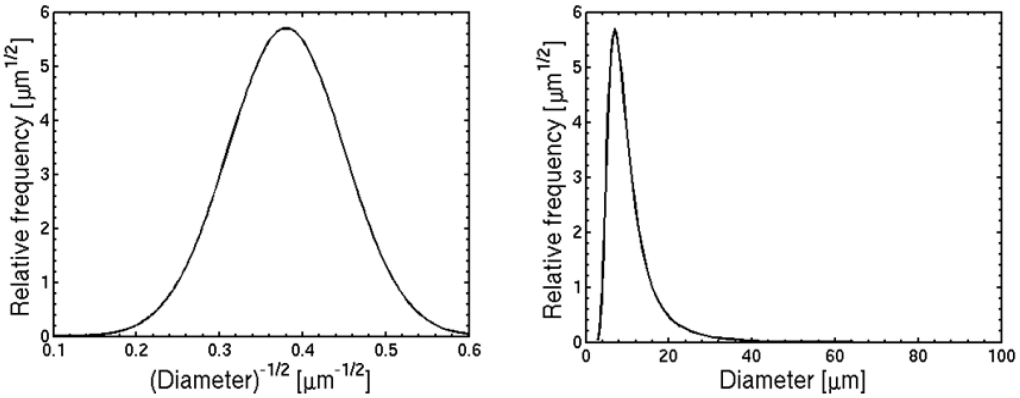

Figure 3.1: Probability density function (pdf) used for assigning the vessel diameters. The pdf is a Gaussian distribution in terms of $1/\sqrt{\text{diameter}}$ (a) and skewed when plotted in terms of the diameter (b) with a peak at approximately 7 μm.

Unlike in MC simulations, the voxel was discretized isotropically into $N \times N \times N$ *subvoxels*. For each voxel, two maps were created: one was a vessel map, **V**, defined to

be 1 for each subvoxel occupied by a blood vessel and 0 everywhere else; the other was a frequency offset map, $\boldsymbol{\Delta\omega}$, which was given by the product of the gyromagnetic ratio, γ, and the field offset for a cylinder given by Eq. (2.36). $\mathbf{V}$ and $\boldsymbol{\Delta\omega}$ were computed using the centre coordinate of each subvoxel, not by averaging over each subvoxel. dCBV can be determined from $\mathbf{V}$ by summing over all of its elements:

$$\mathrm{dCBV} = \frac{1}{N^3}\sum_{l,m,n} V_{lmn}. \tag{3.1}$$

This value of dCBV was usually not equal to the value of dCBV requested because the vessels were never completely homogeneously distributed; therefore, the requested dCBV is referred to as the *nominal* dCBV. An example vessel network and its frequency offset map are shown in Figure 3.2.

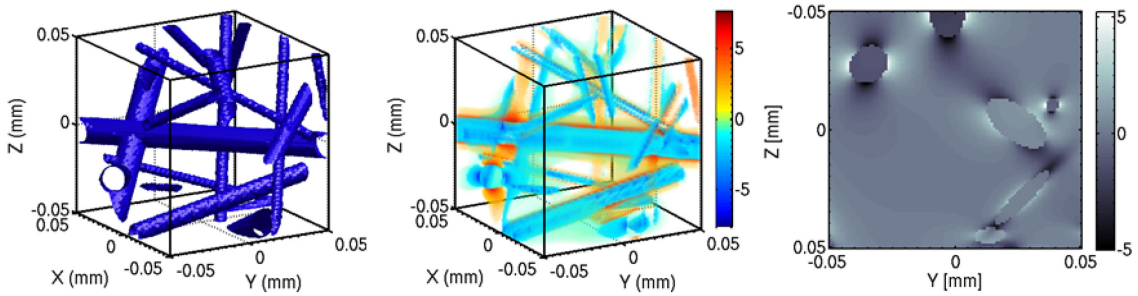

Figure 3.2: 3D rendering of a vessel network (a) and its corresponding frequency offset map (b). A 2D slice of the frequency offset map in the *yz*-plane is shown in (c). The colour bars in (b) and (c) are both in units of Hz and were produced using the standard physiological settings in Table 3.1.

In both the 2D and 3D models of deterministic simulation, the complex valued transverse magnetization matrix, $\mathbf{M}$, is operated on in discrete time steps, δt, by a diffusion kernel $\mathbf{D}$ and a relaxation and precession matrix $\mathbf{R}$. At the j-th time step, $\mathbf{M}$ is given by

$$\mathbf{M}_j = \left(\mathbf{M}_{j-1} * \mathbf{D}\right) \cdot \mathbf{R}, \tag{3.2}$$

where $*$ represents convolution and $\cdot$ represents element-wise multiplication. Like in most MC simulations, the transverse magnetization is simulated immediately following the 90° excitation and it is initially coherent and of unit magnitude, i.e., $M_{lmn,0} = 1 \; \forall \; (l,m,n) \in [1,N]$, where l, m, and n represent the 3D matrix indices and the 0 indicates the initial time point. Each subvoxel of **R** is given by

$$R_{lmn} = e^{-i\Delta\omega_{lmn}\delta t} \times \begin{cases} e^{-\delta t/T_{2,t}} & \text{in tissue } (V_{lmn} = 0) \\ e^{-\delta t/T_{2,b}} & \text{in blood } (V_{lmn} = 1) \end{cases} \tag{3.3}$$

where $T_{2,t}$ is the T_2 of tissue (specifically GM) and $T_{2,b}$ is the T_2 of blood. In this thesis, T_2 decay was ignored in order to only examine susceptibility-related effects; however, although not used, finite T_2 values were incorporated into the simulations, where a T_2 of 110 ms was used for GM [62] and the T_2 of blood was calculated using an empirically determined quadratic relationship between R_2 and S_bO_2 at 3 T [59]:

$$T_{2,b}^{-1} = R_{2,b} = A + B(1 - S_bO_2) + C(1 - S_bO_2)^2. \tag{3.4}$$

A, B, and C in Eq. (3.4) are dependent on the Hct value, so they were linearly interpolated from the experimental values in [59] for the values of Hct used in the simulations.

Bandettini and Wong [22] chose to represent diffusion as a smoothing process by convolving **M** with a Gaussian kernel. In light of the theory presented in Section 2.4.1 on molecular diffusion, this makes sense since the diffusion of an ensemble of spins will be Gaussian distributed and one can consider the transverse magnetization of each subvoxel to represent an ensemble of spins. For a subvoxel with indices l, m, and n and corresponding coordinates (x_l, y_m, z_n), the diffusion kernel was given by

$$D_{lmn} = \left(\frac{\Delta x}{\sqrt{4\pi D\delta t}}\right)^3 \exp\left[-\frac{x_l^2 + y_m^2 + z_n^2}{4D\delta t}\right], \tag{3.5}$$

where D is the diffusion coefficient and $\Delta x = W/N$ is the subvoxel width. Furthermore, **D** is separable into three identical 1D kernels allowing independent convolution along each dimension, making the convolution much more efficient. The 1D kernel was given by

$$D_l = \frac{\Delta x}{\sqrt{4\pi D \delta t}} \exp\left[-\frac{x_l^2}{4D\delta t}\right]. \tag{3.6}$$

To make the convolution even more efficient, the kernel size was cut off at a half-width of 5σ (rounded up to the nearest subvoxel). At this size, over 99.9999% of the area under the Gaussian was accounted for and the kernel length was typically $\ll N$. Depending on the particular combination of D, δt, and Δx, the kernel could be greater than 1 at its origin, which would lead to an increase in the signal. To counter this, the kernel was always normalized by the sum of all of its elements.

Finally, the signal magnitude at the j-th time point was given by

$$S_j = \frac{1}{N^3}\left|\sum_{l,m,n} M_{lmn,j}\right|. \tag{3.7}$$

The operations of convolution and multiplication in Eq. (3.2) were repeated up to the desired duration of time for simulating the signal time course. To simulate a spin echo sequence, **M** was replaced by its complex conjugate at the step corresponding to the 180^o pulse.

All simulations were run in MATLAB (MathWorks, Natick, MA) with the slower running functions for creating the vessel and frequency offset maps programmed in C with the MEX library such that they could be run much more quickly but still as MATLAB functions.

3.2 Simulations without Diffusion

The predictions made by Yablonskiy and Haacke [60] regarding the SDR signal equation should be verifiable using these deterministic simulations with no diffusion. Specifically, measurements of R_2' and dCBV obtained by fitting the simulated signals and using Eqs. (2.47) and (2.48), respectively, can be compared with the theoretically predicted values of R_2' given by Eq. (2.45) and the known values of dCBV given by (3.1). The standard settings used in most simulations are summarized in Table 3.1.

Effect of Subvoxel Size

Before verifying the Yablonskiy and Haacke predictions, the effect of subvoxel size was examined by simulating the SE signal using a variety of sizes for the same vessel network. Eight different vessel networks with a nominal dCBV of 3% were created and subvoxel sizes were varied for each network from 1 μm to 10 μm. In order to simulate the signal with smaller subvoxels while remaining within memory constraints, all simulations used a relatively small voxel size of 0.5 mm isotropic. The simulations used mostly the same parameters as listed in Table 3.1 except for S_bO_2, which was varied from 0.2 to 0.8, not because it is necessarily a realistic range, but in order to also examine the effect of the perturber strength.

The effect of subvoxel size was quantified by comparing the fits of R_2' and dCBV at the lower resolutions to the fits with 1 μm subvoxels. Additionally, the entire time series at lower resolutions were compared to the 1 μm resolution time series using the root mean square error (RMSE) defined as

$$\text{RMSE} = \sqrt{\frac{1}{N}\sum_t \left(S_t - S_t^{\text{ref}}\right)^2}, \tag{3.8}$$

where S_t^{ref} is the reference signal obtained in the 1 μm simulation. All signals were initially normalized to 1.

The timing parameters – δt, TE, and t_{final} (the final time point to be simulated) – were chosen to provide a sufficient number of time points for fitting the different time domains of the signal and so that an equal number of time points could be used in each domain. Fitting was done only about the SE since, in the absence of diffusion, fitting around the refocusing pulse and fitting around the SE gave roughly the same values for R_2' and dCBV and since, in practice, this method would be insensitive to refocusing pulse imperfections and the EV contribution to the signal would be less significant. To fit only the linear exponential region of the signal time series, fitting was done from TE/2 to TE - $2t_c$ and from TE + $2t_c$ to t_{final}.

Effect of dCBV

To test the theoretical predictions of Yablonskiy and Haacke, simulations were performed on voxels with increasing values of dCBV and with no IV signal. The nominal values of dCBV used were 0.2%, 0.5%, 1%, 3%, 5%, and 7%. A 1.5 mm voxel with 256^3 subvoxels was used ($\therefore$ subvoxel width Δx = 3.9 μm).

For each value of dCBV, eight different vessel networks were constructed and the average relative errors in the estimated R_2' and dCBV with respect to theory were calculated.

Table 3.1: Standard simulation parameters (unless stated otherwise in the text).

Simulation parameter	Standard value
Gyromagnetic ratio of ^{1}H (γ)	2.67513×10^8 rad · s^{-1} · T^{-1}
Field strength (B_0)	3 T
Time increment (δt)	1.0 ms
Echo time (TE)	80 ms
Total simulation time (t_{final})	120 ms
Susceptibility difference between fully deoxygenated and fully oxygenated blood ($\Delta\chi_{do}$)	0.264 ppm [63]
Blood oxygen saturation (S_bO_2)	0.60
Hematocrit (Hct)	0.42

Large Numbers Assumption

A consequence of the large numbers condition that the Yablonskiy and Haacke theory is dependent on is that the relative precision of the estimates of R_2' and dCBV should be proportional to $1/\sqrt{N_{ves}}$, where N_{ves} is the number of vessels in the voxel. This was examined by calculating the standard deviations of the relative errors on R_2' and dCBV obtained in the previous section where dCBV was systematically increased (and therefore N_{ves} too). These standard deviations were then plotted against $1/\sqrt{N_{ves}}$.

3.3 Simulations with Diffusion

Given the complex nature of the simulations when incorporating diffusion with the vascular effects, more basic validations were first performed on a completely homogeneous voxel in a linear gradient. Afterwards, simulations were done on vascular networks to see how their results compared to the homogeneous voxel case and how they could potentially be improved.

3.3.1 Homogeneous 1D Voxel in a Linear Gradient

The theory for the spin echo signal in the presence of a linear gradient was rigorously explored by Carr and Purcell [64]. A decade later, by solving the Bloch-Torrey equation, Stejskal and Tanner [65] derived a solution for the transverse magnetization that extended the theory of Carr and Purcell to the use of arbitrary gradients. Using this general solution, it can be shown that under a constant linear gradient G applied along one dimension, the time series of a spin echo sequence is described by

$$S(t) = \begin{cases} e^{-\gamma^2 G^2 D t^3/3} \left|\mathrm{sinc}\left(\gamma G \frac{W}{2} t\right)\right| e^{-\frac{t}{T_2}}, & 0 \le t \le \frac{\mathrm{TE}}{2} \\ \exp\left\{-\gamma^2 G^2 D \left[\frac{1}{3}t^3 - \mathrm{TE}\left(t^2 - \frac{\mathrm{TE}^2}{4}\right) + \mathrm{TE}^2\left(t - \frac{\mathrm{TE}}{2}\right)\right]\right\} & \\ \quad \times \left|\mathrm{sinc}\left[\gamma G \frac{W}{2}(TE - t)\right]\right| e^{-t/T_2}, & t \ge \frac{\mathrm{TE}}{2} \end{cases} \tag{3.9}$$

where W is the voxel width and D is the diffusion coefficient. At the SE, Eq. (3.9) simplifies to

$$S(t = \mathrm{TE}) = e^{-\gamma^2 G^2 D \mathrm{TE}^3/12} e^{-TE/T_2}, \tag{3.10}$$

the same equation derived by Carr and Purcell [64]. Eqs. (3.9) and (3.10) provide a direct method for validating the simulations in their entirety or at just the SE. In the case of free induction decay, the signal just follows the first line of Eq. (3.9) for all time. An example theoretical time series is plotted in Figure 3.3 with two different gradient strengths.

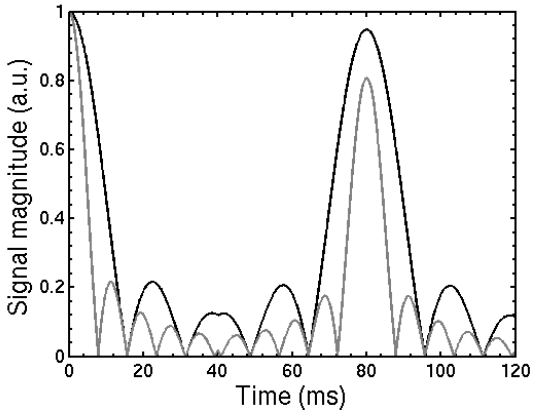

Figure 3.3: Plots of Eq. (3.9) for a 1.0 mm voxel with TE equal to 80 ms, D equal to 0.8 μm^2/ms, and the linear gradient equal to 5 mT/m (black line) and 10 mT/m (grey line).

To immediately simplify and accelerate the simulations, they were conducted in 1D instead of 3D. This was possible since the voxels were homogeneous and a linear gradient was applied along one direction. Both 1D and 3D simulations produced the exact same results (results not shown). The diffusion kernel stayed the same as in Eq. (3.6) but, ignoring T_2 effects, the relaxation and precession matrix/vector **R** was given by [23]

$$R_l = \exp[-i\gamma G x_l \delta t] \tag{3.11}$$

where x_l is the subvoxel coordinate of the l-th subvoxel.

Signal Analysis

In the following sections, simulations were compared with the theoretical time series given by Eq. (3.9) using the RMSE (see Eq. (3.8)). Additionally, it was observed that often the simulated and theoretical time series were in excellent agreement *except* for at the SE. For this reason, the error at the SE was also used as a metric of comparison.

Convolution Edge Effects

For convolving **M** with **D**, both the explicit formula for convolution (summation and multiplication) and Fourier transform-based circular convolution were tested and the explicit method was found to run more quickly than the Fourier-based method in both 1D

and 3D due to the need to take both the forward and inverse Fourier transform of **M** at every iteration (results not shown). Since convolution assumes zero transverse magnetization outside of the voxel and it will produce non-zero values outside of the voxel, edge effects had to be mitigated by sampling only an inner, central subset of **M**. Therefore, for a voxel width W and an unsampled edge width of w, the new sampled voxel size was $W' = W - 2w$. Note that the width W' replaces W in Eq. (3.9).

The required unsampled edge width was determined by using a constant sampled voxel size of 1.0 mm (i.e. $W' = 1.0$ mm) and constant subvoxel size of 1.0 μm and incrementally augmenting the unsampled edge width. The other simulation parameters were the same as the standard parameters in Table 3.1 (the first five were applicable) plus two different values for D and multiple gradient strengths were used.

The results from this (see section 4.2.1) showed that an unsampled edge width of 0.1 mm was more than adequate for the simulation parameters used and the range of D in GM.

Effect of the Diffusion Coefficient and Time Increment

The range of D values needed in simulations is clearly dictated by biology. In the case of GM, the approximate minimum and maximum values stated in the literature are 0.7 $\mu m^2/ms$ and 1.2 $\mu m^2/ms$ with an average ~ 0.8 $\mu m^2/ms$ [66-69]. To evaluate this range of values, simulations were performed from D = 0 $\mu m^2/ms$ up to 2 $\mu m^2/ms$ with several subvoxel sizes and gradient strengths using the standard simulation parameters in Table 3.1. As described in the previous section, an unsampled edge width of 0.1 mm per edge was used with a total voxel width of 0.5 mm (i.e. the central 0.3 mm were sampled).

To examine the combined relationship of D and the time increment, δt, on the diffusion kernel width (see Eq. (3.5) or (3.6)), the two of them were independently doubled and halved. Thus, using D = 0.7 $\mu m^2/ms$ and δt = 1.0 ms as the common setting, D was set to 0.35 $\mu m^2/ms$ and 1.4 $\mu m^2/ms$ while δt remained fixed at 1.0 ms and, similarly, δt was set to 0.5 ms and 2.0 ms while D remained fixed at 0.7 $\mu m^2/ms$. Simulations using the standard parameters were performed on a 0.5 mm voxel using a

broad range of subvoxel sizes and gradient strengths (see the next subsection for more details on the exact values used).

Effect of Subvoxel Size and Gradient Strength

Clearly, the subvoxel size will have a significant impact on the simulation accuracy; if it is too large, the Gaussian distribution for the diffusion kernel will be undersampled, making it behave more like a delta function such that the smoothing of **M** at each step will be negligible. Figure 3.4 illustrates this.

To investigate the effect of subvoxel size on the accuracy of the simulations, the subvoxel size and the linear gradient strength were independently varied from 5 μm down to 0.5 μm and from 0 mT/m up to 700 mT/m, respectively. Although a gradient as large as 700 mT/m across an entire voxel is unrealistic, the local gradients around the smallest blood vessels can be as large as up to 1200 mT/m, therefore a wide range of gradient strengths was tested[6]. The total voxel width was 0.5 mm and simulations were done with δt = 1 ms, SE TE = 20 ms, 40 ms, 60 ms, and 80 ms, and with D set to 0.7 μm^2/ms and 1.2 μm^2/ms.

3.3.2 Simulations with Vessel Networks

When adding diffusion into vessel network simulations, the issues of IV signal and vessel permeability must be carefully considered. To simplify matters, the simulations included IV signal, assumed free permeability at the vessel walls, and T_2 decay was ignored. Including IV signal and assuming free permeability permitted convolution of **M** with **D** without any special consideration for IV/EV contributions.

Without any *general* theoretical signal equation against which the simulations could be compared, simulations were run in vessel networks using successively smaller subvoxel sizes with the goal of observing a convergence in the signals. This was done using the same eight 3D vessel networks that were used for the earlier evaluation of the

[6] This gradient strength was estimated by finding the change in ΔB in Eq. (2.36) experienced by a proton diffusing its root mean diffusion distance $\sqrt{\langle r^2 \rangle} = \sqrt{2D\delta t}$ outside the smallest vessel (radius = 1.39 μm) with the standard settings from Table 3.1 and $D \sim 0.8$ μm^2/ms.

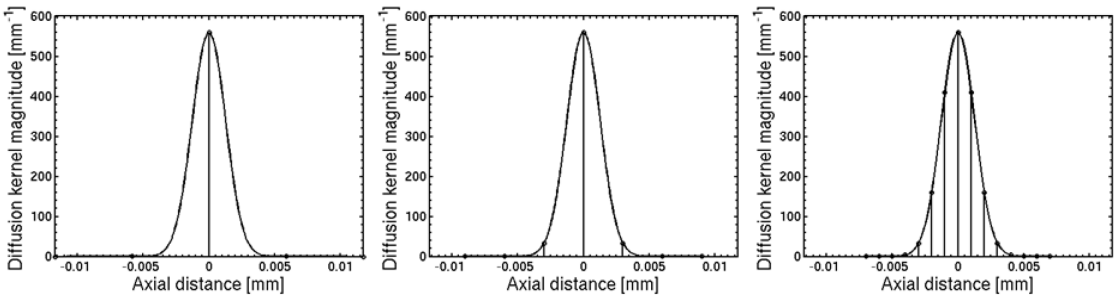

Figure 3.4: Effect of subvoxel size on the diffusion kernel. Subvoxel size equals 5.9 μm (a), 3 μm (b), and 1 μm (c). In each plot, the solid curve shows the theoretical Gaussian probability distribution given by Eq. (2.32) and the data points and stems show the sampled kernel given by Eq. (3.6) divided by the subvoxel width. The examples shown use D = 0.8 μm^2/ms and δt = 1 ms.

effect of subvoxel size in Section 3.2. These networks were 0.5 mm wide, therefore only the central 0.3×0.3×0.3 mm^3 were sampled. D was set to 0.7 μm^2/ms and the standard simulation settings in Table 3.1 applied except for S_bO_2, which was varied from 0.2 up to 0.8 in 0.2 increments. As before, subvoxel size was varied from 1 μm to 10 μm and all signals were compared to the 1 μm signal using the RMSE and the error at the SE. Furthermore, two different solutions for R_2' were obtained for each simulated signal by fitting about the refocusing pulse and about the SE assuming linear exponential decay on long time scales.

3.3.3 Scaling the Diffusion Coefficient for Signal Optimization

As mentioned above, if the subvoxel size is too large, the diffusion kernel loses its ability to sufficiently blur **M**. One might therefore still attribute the less substantial signal loss to diffusion but with a lower effective D. This observation, combined with the constant desire to increase simulation speed, led to the investigation of finding a diffusion scaling factor, ψ_D, for low resolution simulations that, when multiplied with D in the diffusion kernel, would best simulate the desired signal. Therefore, all instances of D in the diffusion kernel were replaced by $D' = \psi_D D$, with ψ_D expected to be greater than or equal to 1.

In the homogeneous 1D voxel, ψ_D was determined by minimizing the RMSE between the simulated signal and the theoretical signal, with fixed diffusion coefficient *D* and gradient *G*, using the *fminbnd* function in MATLAB to vary ψ_D based on golden section search and parabolic interpolation. ψ_D was allowed to vary between 0.9 and 5.0. This was performed with a SE TE of 80 ms and *D* equal to 0.7 μm^2/ms while the subvoxel size and gradient strength were independently varied. An example optimization for one set of simulation parameters is shown in Figure 3.5, where a marked improvement in the simulation accuracy can be seen.

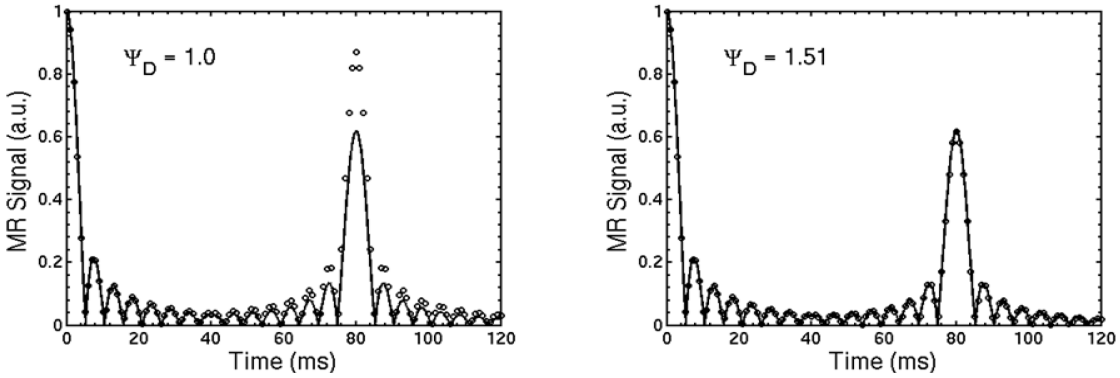

(a) **(b)**

Figure 3.5: Example time series for a non-optimized diffusion scaling factor ψ_D (a) and an optimized ψ_D (b). The theoretical and simulated time series are represented by the solid line and the circles, respectively. Optimization was done with *D* equal to 0.7 μm^2/ms, a gradient strength of 15 mT/m, and a subvoxel size of 3.33 μm. The optimized ψ_D was 1.51 and improved the RMSE from 5.24×10^{-2} to 2.60×10^{-4}.

Unlike the 1D case, determining the optimal ψ_D for 3D vessel networks had to be performed manually since the simulations took much longer. As a result, optimization was only tested on a single vessel network with one particular set of simulation parameters: SE TE = 80 ms, S_bO_2 = 0.6, and target *D* = 0.7 μm^2/ms. The reference signal used was from a 0.5 mm voxel with 1.0 μm subvoxels and ψ_D = 1.0 and the optimization was performed by incrementally increasing ψ_D from 1.0 to 2.0 on the same vessel network but using 2.5 μm subvoxels. The RMSE, absolute error at the SE, percent error

in R_2', and percent error in dCBV were all used for comparison with the 1.0 μm subvoxel size simulation.

Chapter 4 Results

As detailed in the previous chapter, simulations with and without diffusion were separately analyzed since the convolution operation required for diffusion added considerable complexity to the simulations.

4.1 Simulations without Diffusion

4.1.1 Subvoxel Size

In the absence of diffusion, the effect of subvoxel size is fairly insignificant. Figure 4.1a illustrates this through a plot of the differences in the time series at low resolution to the time series obtained at 1 μm for a single vessel network. As one can see, these differences are on the order of 10^{-4} for signals initially normalized to 1, making them essentially too small to see when examining the actual time series themselves. Similar time series were simulated for eight different vessel networks at multiple resolutions and multiple values

of S_bO_2. When averaged over the eight different networks, the RMSE increased approximately exponentially from a subvoxel size of 1 μm to 5 μm (see Figure 4.1b). Beyond 5 μm, the RMSE appeared to increase more linearly. For all subvoxel sizes, the RMSE almost invariably increased as the oxygen saturation decreased, or, looked at another way, it increased as the perturber strength increased (since the perturber strength is proportional to 1 - S_bO_2).

From Figure 4.1c and d, the average relative errors in R_2' and dCBV did not vary greatly up to a subvoxel size of 2.5 μm but beyond that, they started to show perhaps some systematic error. Unlike the RMSE, the relative errors in R_2' and dCBV did not show a clear monotonic relationship with oxygen saturation; they both seemed to increase up to a point as S_bO_2 increased and then proceeded to decrease.

4.1.2 dCBV and the Number of Vessels

The effect of increasing dCBV on the estimates of R_2' and dCBV are shown in Figure 4.2a and b. Overall, for all values of S_bO_2, the relative errors on R_2' and dCBV were relatively constant (within uncertainties) with respect to dCBV except for outliers at dCBV ≈ 0.6 %. As a verification of the Yablonskiy and Haacke theory, the linearity between the precision of the estimates of R_2' and dCBV versus the number of vessels was tested. Figure 4.2c and d show plots of the standard deviations of the relative errors in R_2' and dCBV versus $1/\sqrt{N_{ves}}$ and their corresponding linear fits that pass through the origin are also plotted. The data points follow a fairly linear trend except for outliers located near 0.014 (corresponding to an average dCBV of 6%). The results from those fittings are summarized in Table 4.1.

Furthermore, by plotting the *analytical* time series given in Eq. (2.41) with the known dCBV for each vessel network and then solving for R_2' and dCBV by fitting the linear exponential time domains in the same manner as for the simulated time series, the fitted values still did not give the analytically expected results for R_2' (Eq. (2.45)) and the known dCBV (see Figure 4.3). However, for a given S_bO_2, every vessel network had the *exact same* relative error in the fitted values of R_2' and dCBV, indicating a degree of bias

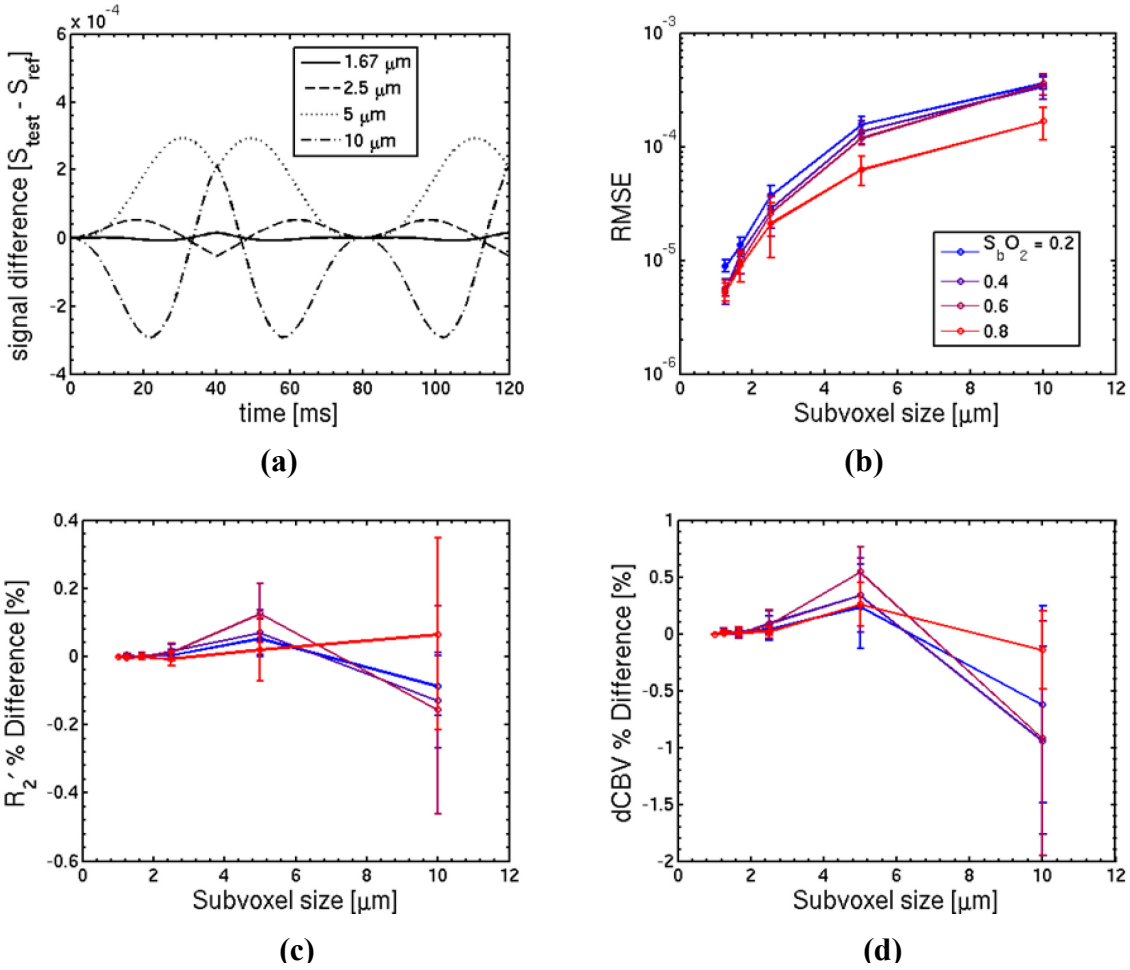

Figure 4.1: Effect of subvoxel size on simulations with vessel networks with no diffusion. An example of the actual differences in time series is plotted in (a) for a vessel network simlulated at an S_bO_2 of 0.6 at five different subvoxel sizes (signal differences are relative to the simulated signal at 1.0 μm). As a function of subvoxel size, the average RMSE (b), average percent difference in R_2' (c), and average percent difference in the estimated dCBV (d) are plotted for four different values of S_bO_2 (all share the same legend as (b)). All of the plots, (a) – (d), are relative to their respective results at 1 μm resolution.

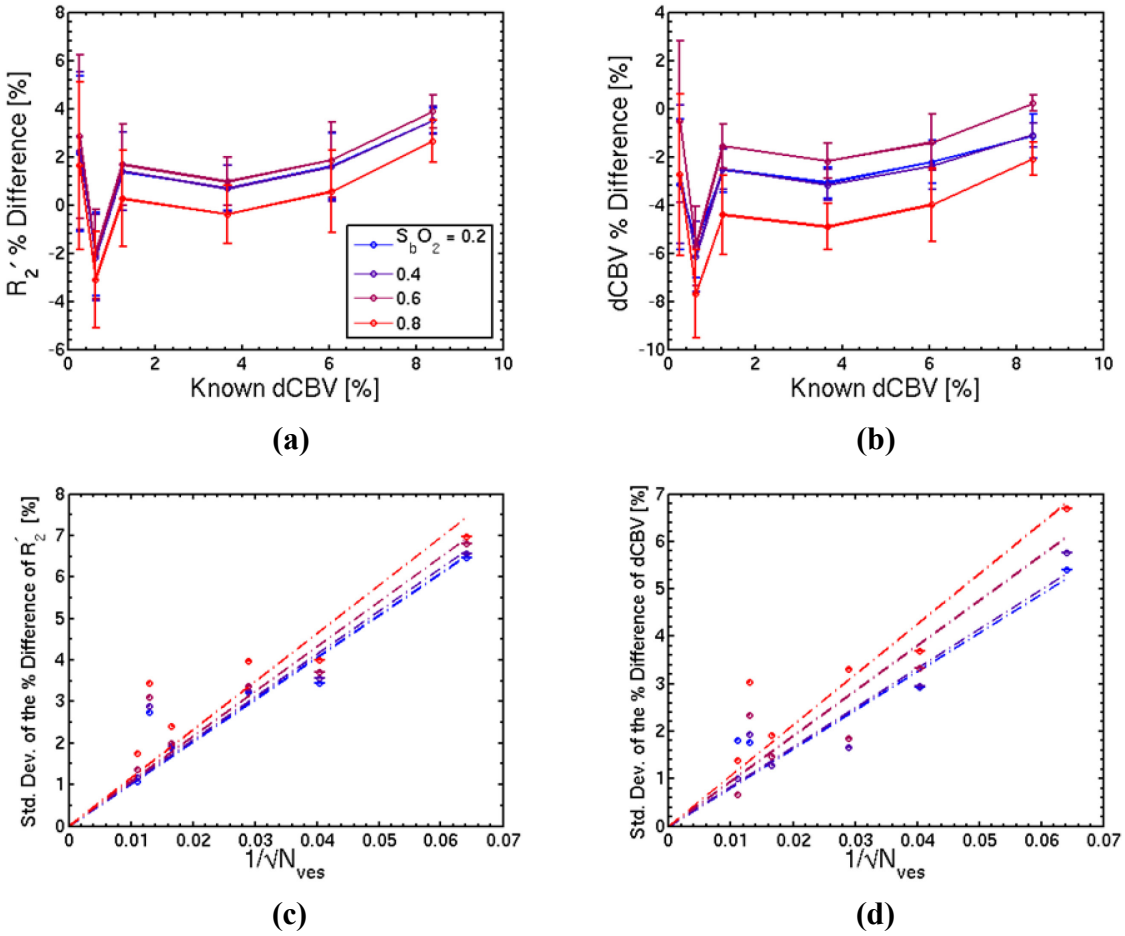

Figure 4.2: The effect of increasing dCBV (or the number of vessels) on the accuracy and precision of the estimates of R_2' and dCBV at various blood oxygen saturation levels. The average relative errors in R_2' (a) and dCBV (b) are plotted as functions of the known dCBVs and their standard deviations are plotted as functions of one over the square root of the number of vessels (N_{ves}) ((c) and (d), respectively). Linear fits are included at each S_bO_2 level in (c) and (d) (dash-dot curves). Since the exact number of vessels varies from one network to the next, horizontal error bars with widths equal to the standard deviations are included and represented as horizontal bars through the markers. In (a) and (b), the standard deviations on the dCBV are smaller than the marker widths and hence not visible, also, the data for S_bO_2 = 0.4 is hardly visible since it is nearly equal to the data at S_bO_2 = 0.2. All figures share the same legend as (a).

in the results. This bias was quite small for R_2' but fairly large for dCBV.

Table 4.1: Results of the linear fits of the form $y = mx$, where y is either the standard deviation of the percent error on R_2' or on dCBV and x is $1/\sqrt{N_{ves}}$. R^2 is the coefficient of determination.

S_bO_2	Linear fits for R_2'		Linear fits for dCBV	
	m [%]	R^2	m [%]	R^2
0.2	102 ± 9	0.848	81 ± 7	0.848
0.4	104 ± 9	0.832	83 ± 7	0.893
0.6	110 ± 10	0.806	95 ± 9	0.877
0.8	120 ± 10	0.677	110 ± 10	0.812

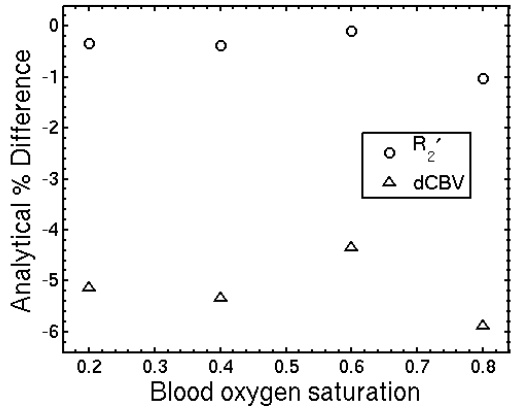

Figure 4.3: Relative error in R_2' (circles) and dCBV (triangles) obtained by fitting the analytical time series from Eq. (2.41) when compared to the analytical solution for R_2' in Eq. (2.45) and the known dCBV. These relative errors were exactly the same for all vessel networks, they only varied with perturber strength (S_bO_2 in this case).

4.2 Simulations with Diffusion

4.2.1 Simulations with a Homogeneous 1D Voxel

Convolution Edge Effects

As mentioned in the Methods section, the act of convolution of **M** with the diffusion kernel leads to corruption of the edge voxels due to the assumption of zero transverse magnetization outside of the voxel. To mitigate this effect, only a central subset of **M** was sampled when diffusion was added to the simulations. The minimum required unsampled edge width was determined by incrementally increasing the edge width and comparing the simulated time series to the theoretically predicted time series from Eq. (3.9) using the RMSE. Shown in Figure 4.4, these simulations were performed for various combinations of gradient strength and D; for each combination, the RMSE converged at some width and this would be considered an appropriate unsampled edge width. Since the width of the diffusion kernel increases with increasing D, a larger unsampled edge width is needed for a high D. For D = 1.0 μm^2/ms, the RMSE converged to within five significant figures by an edge width of 0.08 mm and for D = 2.0 μm^2/ms, it converged by an edge width of 0.1 mm. D = 2.0 μm^2/ms is larger than observed in GM [66-69], therefore, an unsampled edge width of 0.1 mm was used to ensure the edge width was sufficiently large.

One can consider the repeated convolution of **M** with the kernel **D** n times as a single convolution of **M** with an effective kernel $\mathbf{D}_{\mathbf{eff}}(n)$. From linear systems theory, convolution of normally distributed functions with the same mean results in a net function that is also normally distributed with the same mean but with a variance given by the sum of the individual variances. This means that $\mathbf{D}_{\mathbf{eff}}(n)$ is also normally distributed with zero mean but with a variance equal to

$$\begin{aligned} \sigma_{eff}^2(n) &= n\sigma^2 \\ &= n2D\delta t \\ &= 2Dt_{final} \end{aligned} \tag{4.1}$$

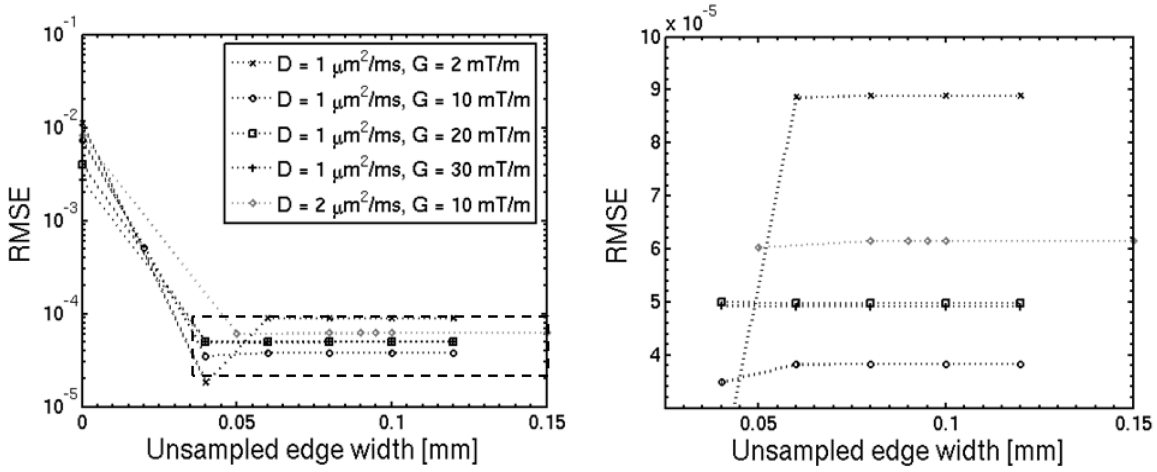

Figure 4.4: Convergence of the RMSE with increasing unsampled edge width for various gradient strength-*D* combinations. The dashed box in (a) is magnified in (b).

The effective 5σ widths for D = 1.0 μm^2/ms and D = 2.0 μm^2/ms when δt = 1.0 ms and n = 120 are 0.077 mm and 0.110 mm, respectively. These values are in excellent agreement with what was found experimentally although the 2.0 μm^2/ms width is slightly larger than found and this is most likely because between 4σ and 5σ, the kernel values are very small (~10^{-6} to 10^{-4}), therefore lessening the need for a larger edge width.

Effect of the Diffusion Coefficient and the Time Increment

The effect of D was examined by varying it from 0 to 2 μm^2/ms and simulating the signal with a range of gradient strengths and subvoxel sizes. The RMSE was then calculated for all simulation parameters and they are shown plotted in Figure 4.5. For all sets of simulation parameters, the RMSE is 0 when there is no diffusion; as D increases away from zero, so too does the RMSE; eventually the RMSE peaks and it returns back down to some lower value as D continues to increase.

This behaviour can be understood by comparing the three different diffusion kernels in Figure 4.6. These kernels were created with the exact same parameters except for D, which went from 0.01 μm^2/ms to 0.1 μm^2/ms to 1.0 μm^2/ms. The kernel in (a) is almost a delta function, so it will underestimate the effect of diffusion; however, at 0.01

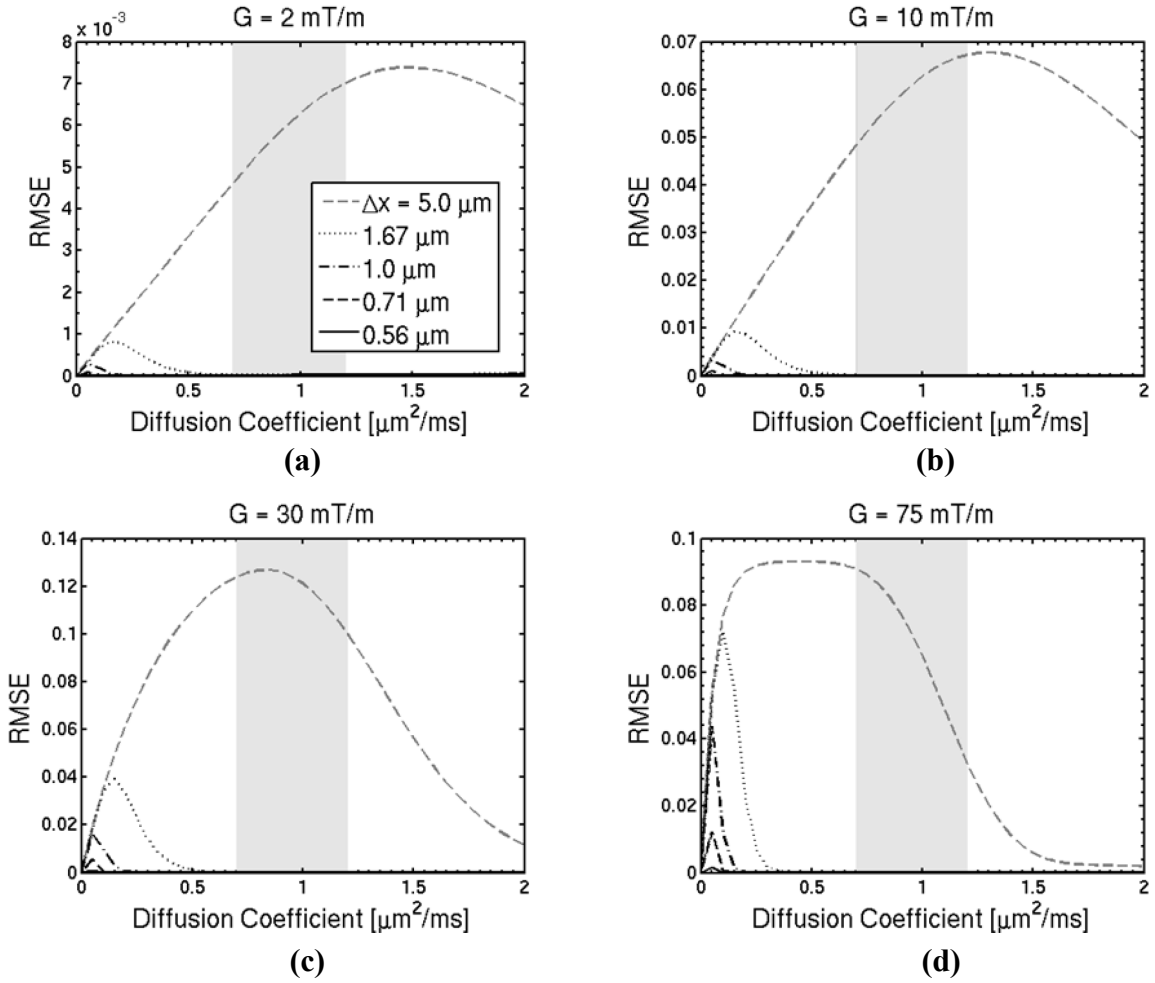

Figure 4.5: Effect of increasing the value of *D* on the RMSE for a range of subvoxel sizes and gradient strengths (indicated by the subfigure titles). All figures share the same legend as (a). The shaded region in each figure delineates the approximate range of *D* in grey matter (0.7 – 1.2 $\mu m^2/ms$). The plot obtained at 0.56 μm subvoxel size is only visible as the very small hump in the bottom left of (d).

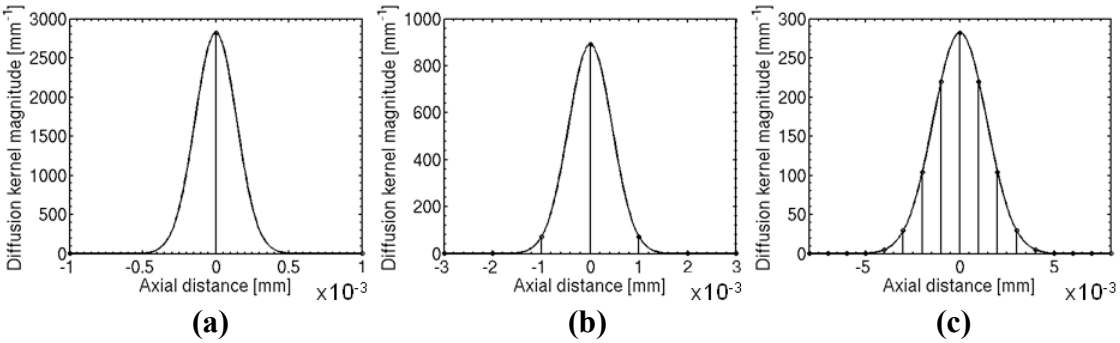

Figure 4.6: Three different diffusion kernels with a subvoxel size of 1.0 μm and time increment of 1.0 ms. D was 0.01 μm^2/ms (a), 0.1 μm^2/ms (b), and 1.0 μm^2/ms (c). In each plot, the solid curve shows the theoretical Gaussian probability distribution given by Eq. (2.32) and the data points and stems show the sampled kernel given by Eq. (3.6) divided by the subvoxel width

μm^2/ms, diffusion will not have much of an effect, therefore, the RMSE will be low. In (b), the kernel is not quite a delta function but it will still do very little smoothing of the transverse magnetization. At this level of diffusion, however, the effect of diffusion in reality will be even stronger, so the RMSE gets even higher. Eventually, the kernel starts to get wide enough (see (c)) such that the Gaussian distribution gets sufficiently sampled and the RMSE proceeds to decrease.

Although not shown, visual agreement between the theoretical and simulated time series did not occur until the RMSE was $\lesssim 10^{-3}$. One can see from Figure 4.5 that for this to be possible with the applicable range of values for D, the subvoxel size must be less than 5 μm. In this case, the RMSE has already peaked and it is decreasing by the time D = 0.7 μm^2/ms is reached. Therefore, to put the most stringent requirements on the validations, all further simulations were done at D = 0.7 μm^2/ms since its RMSE was greatest of all the values of D in the range 0.7 – 1.2 μm^2/ms.

In addition to the individual effects of D on the simulations, the combined effects of D and the time increment, δt, were explored by examining the error at the SE. The error at the SE was used, as opposed to the RMSE, because changing δt changed the number of data points in the time series and therefore also affected the normalization in the RMSE, whereas changing D did not change the number of data points. Therefore, to

compare all of the time series without the additional data points confounding the results, the error at a single point was used.

The results from these simulations are shown in Figure 4.7. By comparing the shapes and positions of the isolines in the subfigures, it is obvious that halving D or halving δt produced qualitatively very similar results on the error at the SE: both shifted the isolines down to smaller subvoxel sizes. Conversely, when the parameters were doubled, the isolines shifted up to larger subvoxel sizes.

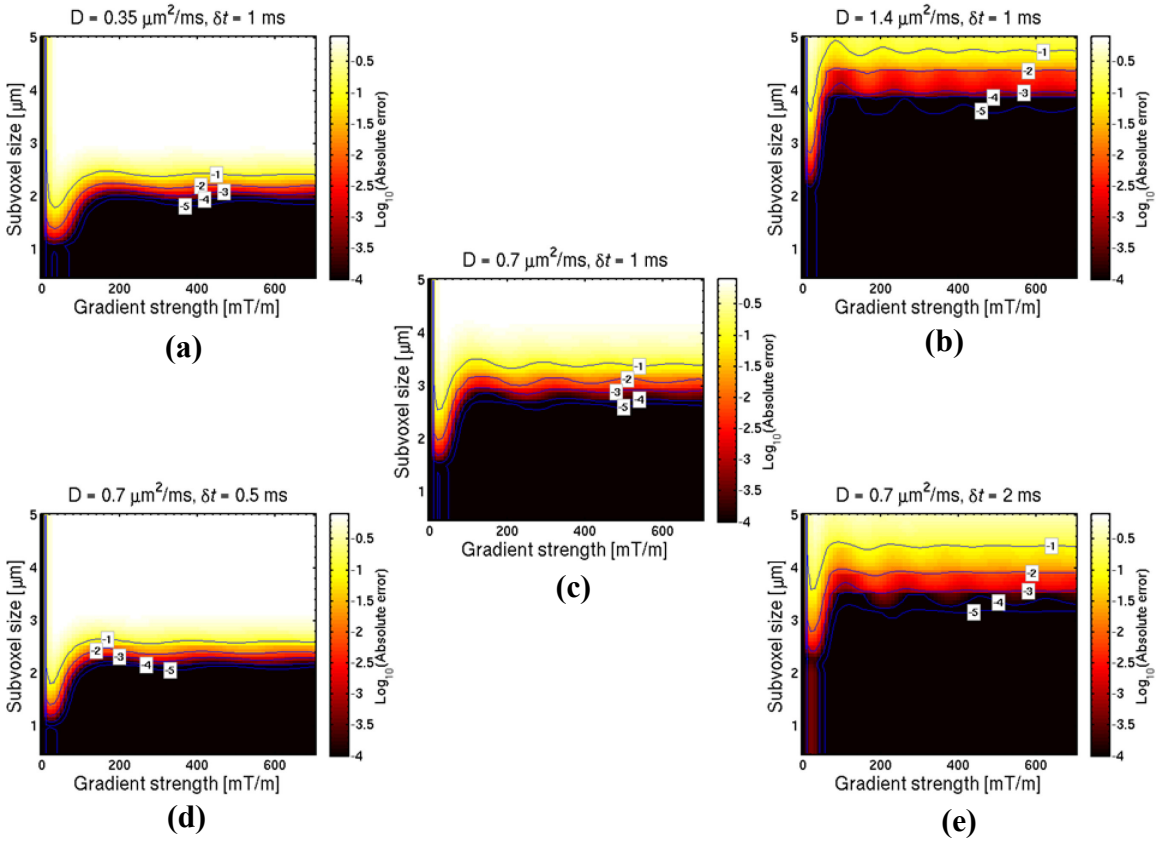

Figure 4.7: The interplay between D and time increment (δt) on the error in the simulations as the gradient strength and subvoxel size are independently varied. Displayed is the log-10 absolute error at the SE and the isolines -1 through -5. In (c), the errors at the SE are shown for the common simulation parameters D = 0.7 μm^2/ms, δt = 1.0 ms. In (a), D was halved and in (b), it was doubled, both while δt remained fixed at 1.0 ms. Conversely, in (d), δt was halved and in (e), it was doubled, both while D remained fixed at 0.7 μm^2/ms.

Effect of Subvoxel Size and Gradient Strength

The final parameters for which the 1D simulations were characterized were the subvoxel size and the gradient strength. These two were independently varied for a range of echo times and with D = 0.7 μm^2/ms, the results of which are shown in Figure 4.8. The simulations were also done with D = 1.2 μm^2/ms but since the RMSE was always greatest for D = 0.7 μm^2/ms, the results are not included.

It is evident from Figure 4.8 that the RMSE isolines have common shapes for all TEs. These shapes gets scaled horizontally (along the gradient strength direction) in proportion to TE. Using Figure 4.8c as a reference, the characteristic features of the isolines include a dip towards smaller subvoxel size from G = 0 mT/m up to some gradient strength (~ 50 mT/m); this is followed by a rise in the subvoxel size until it almost reaches an asymptote (~ 200 mT/m); beyond this, the asymptote moves slightly towards smaller subvoxel size with pseudo-periodic noise added on top of that. The results in the asymptotic region are of little use because at such large gradient strengths, the signal decays away so quickly that it would not even be detectable. Therefore, the most important area to focus on is from zero gradient up to the aymptotic region and, most crucially, the smallest subvoxel sizes that the isolines dip down to within this region. For the four echo times in Figure 4.8, the 10^{-3} isolines all dip down to approximately 2 μm.

These dips in the isolines were further investigated by plotting profiles of the RMSE and the absolute error at the SE at the gradient strengths where the isolines dipped down the lowest (see Figure 4.9). For TE = 20 ms, the gradient strength was 175 mT/m; for TE = 40 ms, the gradient strength was 55 mT/m; for TE = 60 ms, the gradient strength was 30 mT/m; and for TE = 80 ms, the gradient strength was 25 mT/m. On a semi-log scale, both shapes are sigmoidal with plateaus at small and large subvoxel sizes but since the *absolute* error at the SE is plotted, that curve displays a minimum where the simulated and theoretical signals cross. What is important to note here is that even though the RMSE for all TEs reached 10^{-3} by 2 μm, the error at the SE was an order of magnitude

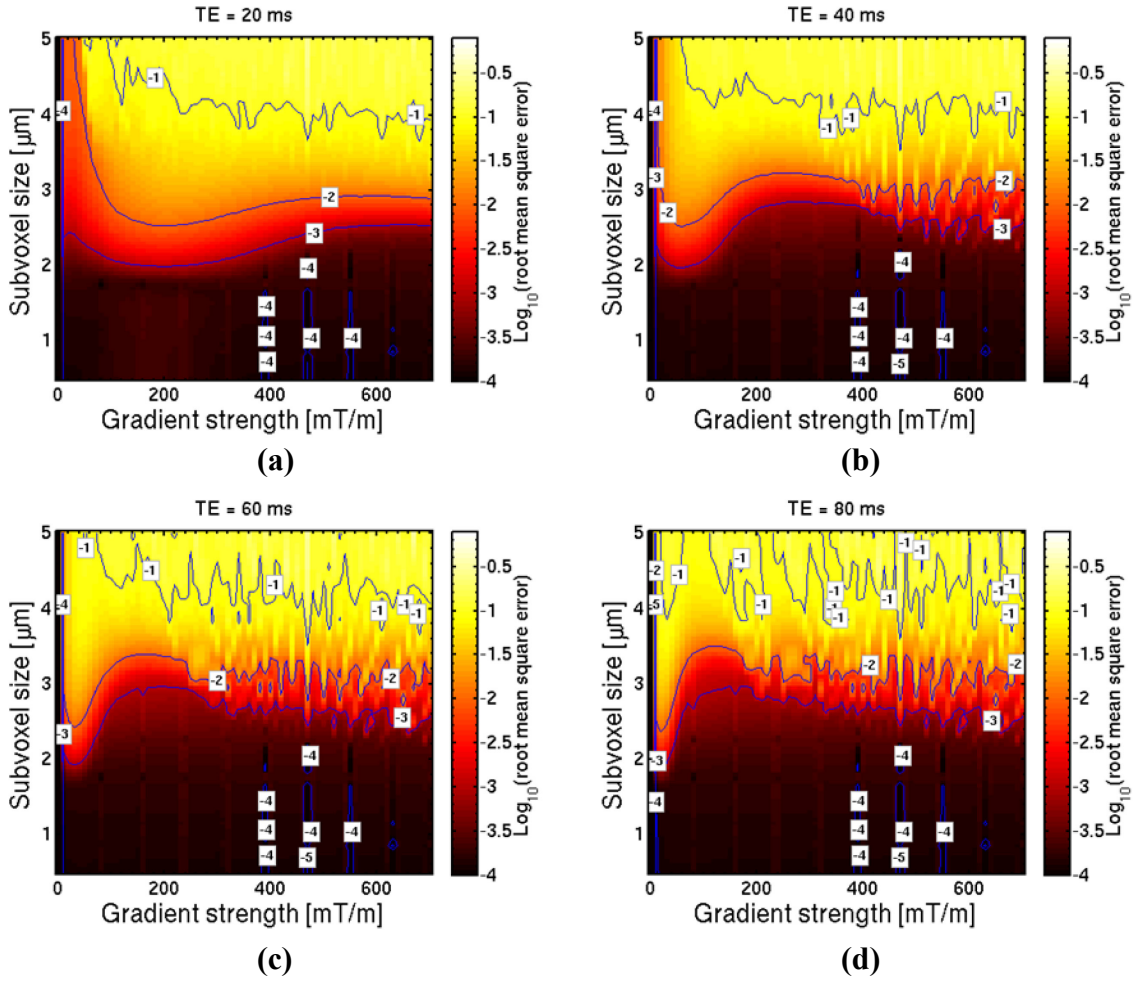

Figure 4.8: 2D colour plots of the RMSE with isolines (blue lines + labels) for four different echo times as the gradient strength and subvoxel size are independently varied. Note that it is actually $\log_{10}$(RMSE) that is plotted and the isolines therefore represent the base-10 exponent of the RMSE.

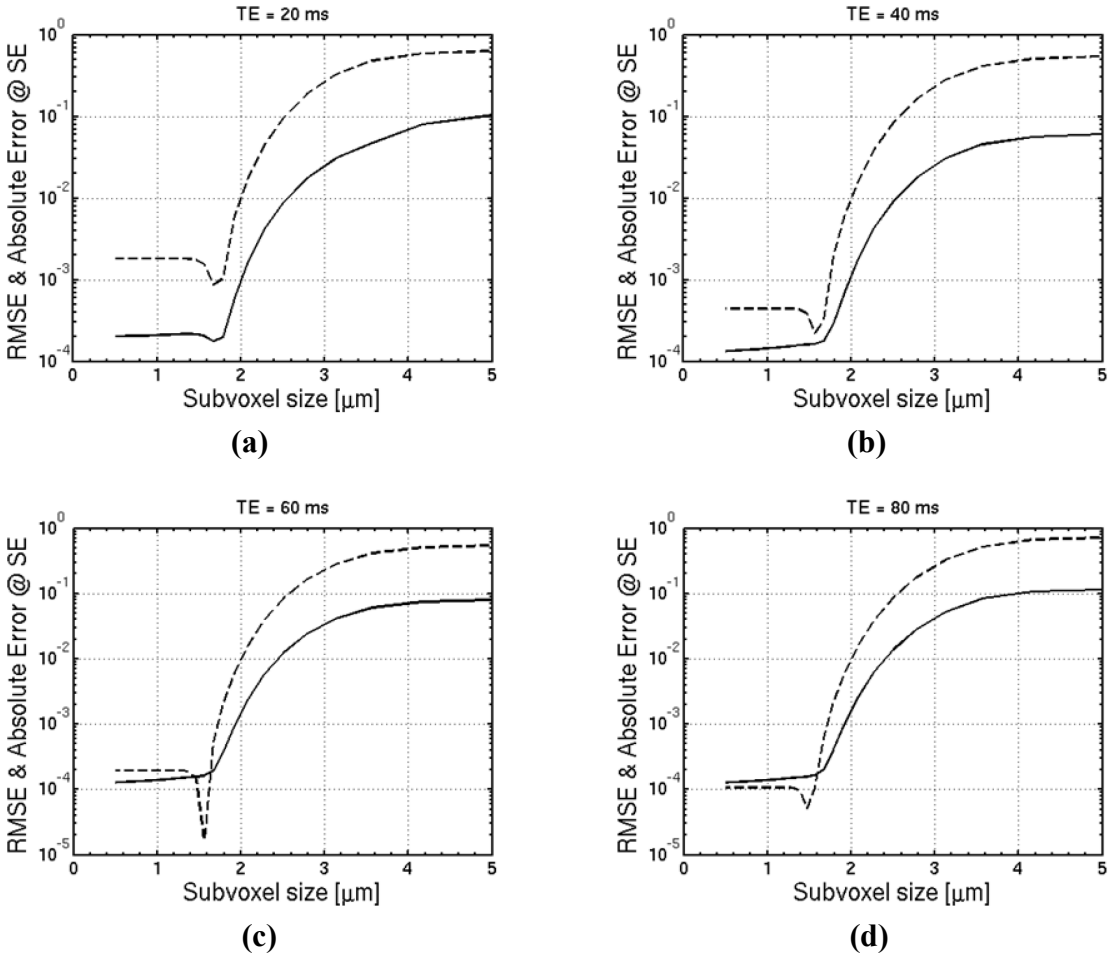

Figure 4.9: RMSE (solid lines) and the absolute error at the SE (dashed lines) plotted against subvoxel size using the gradient strengths where the RMSE isolines in Figure 4.8 dipped the lowest for each TE.

larger. For all TEs, the RMSE reached its lower plateau by approximately 1.7 μm, at which point the error at the SE was then below 10^{-3} (except for TE = 20 ms which plateaued at approximately 2×10^{-3}).

4.2.2 Simulations with Vessel Networks

To observe the effects of diffusion on 3D simulations with vessels, a similar set of simulations was run as before when diffusion was not included. This time, D was fixed at 0.7 $\mu m^2/ms$ and the simulation results were averaged over eight vessel networks at multiple subvoxel sizes and blood oxygen saturations. The subvoxel size now plays a much more significant role in the simulations; this is illustrated in Figure 4.10a where the simulations from a single vessel network are plotted. Below 2 μm, the time series were essentially indistinguishable from the 1 μm time series. The averages of the simulations are summarized using the RMSE (Figure 4.10b), the absolute percent difference in R_2' when fit about the SE (Figure 4.10c), and the absolute percent difference in R_2' when fit about the refocusing pulse (Figure 4.10d). The 1 μm simulation time series were used as the reference signals for the RMSE and the fitted values of R_2' at 1 μm were used for finding the relative errors in R_2' for the larger subvoxel sizes.

The convergence of the RMSE and R_2' percent errors with decreasing subvoxel size were largely independent of the blood oxygen saturation. As in the case of no diffusion, the RMSE decreased as the oxygen saturation increased but, somewhat counter intuitively, the R_2' percent errors increased with the oxygen saturation, particularly for R_2' fit about the refocusing pulse. Above 2 μm, the R_2' percent errors for both fitting methods were biased towards overestimated values since their means plus standard deviations did not cross zero percent. These results are not surprising given that the homogeneous 1D voxel simulations from the previous section showed convergence of the RMSE at approximately 1.7 μm.

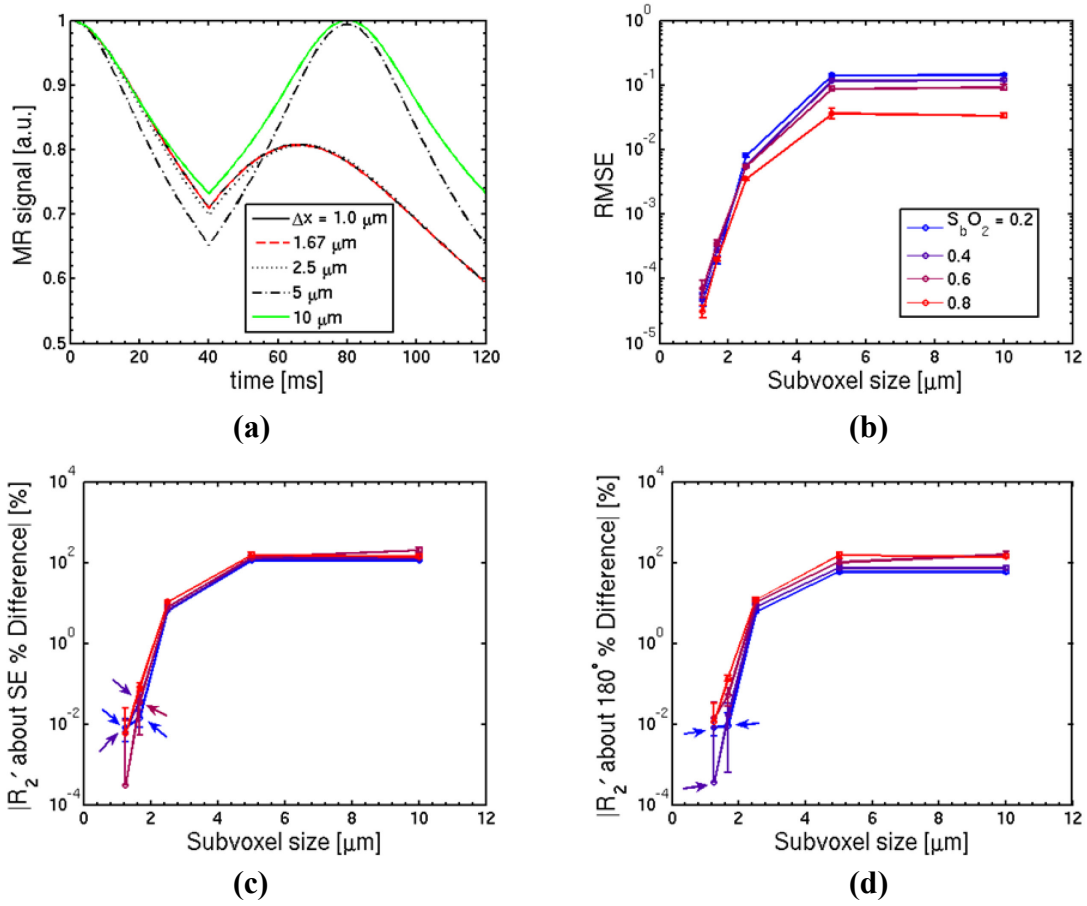

Figure 4.10: Effect of subvoxel size on simulations run with D = 0.7 μm^2/ms in vessel networks. Examples of the actual time series are plotted in (a) for a vessel network simlulated wtih an S_bO_2 of 0.6 at five different subvoxel sizes. As a function of subvoxel size, the average RMSE (b), average percent difference in R_2' when fit about the SE (c), and average percent difference in R_2' when fit about the refocusing pulse (d) are plotted for four different values of S_bO_2 (all share the same legend as (b)). The plots (b) – (d) are relative to their respective results at 1 μm resolution. In (a), the plots from 1.0 μm and 1.67 μm are overlapping. In (c) and (d), the absolute values of the average errors are plotted in order to plot them on a logarithmic scale, negative values are indicated by the arrows. As a result of this, where the lower bounds of the error bars went negative, only the upper halfs were plotted.

4.2.3 Scaling the Diffusion Coefficient

Signal Optimization in 1D

Non-linear signal optimization using a diffusion scaling factor was tested on a 0.5 mm 1D voxel over a range of subvoxel sizes and gradient strengths with D equal to 0.7 μm^2/ms. The optimized diffusion scaling factors, ψ_D, and the resultant RMSEs are shown in Figure 4.11. ψ_D typically increased with subvoxel size and gradient strength but there were also areas where it would jump. The optimized RMSE was relatively constant for a given subvoxel size but it was largely dependent on the subvoxel size, resulting in horizontal banding in the figure. The width of the banding appears to decrease as the subvoxel size decreases but this is only because it was actually the *number* of subvoxels that was explicitly varied (from 100 to 1000 in increments of 10) and the subvoxel size is inversely proportional to this so the data points get closer together as the subvoxel size decreases.

Comparing the optimized and non-optimized RMSE (where ψ_D was held constant at 1.0), one can see that, overall, optimization significantly decreased the RMSE; however, for particular subvoxel sizes, the optimization failed. This is most easily seen in Figure 4.11d since the blue to red colour map shows where the optimized RMSE was better than the non-optimized RMSE and the figure is clearly dominated by blue to red, not black to tan.

Optimization in 3D

Optimization in 3D was performed manually on a single vessel network with 2.5 μm subvoxels and with a target signal produced with 1.0 μm subvoxels, D = 0.7 μm^2/ms, S_bO_2 = 0.6, and SE TE = 80 ms. The target signal and some example test signals along with the comparison results are shown in Figure 4.12. From these results there was no single value of ψ_D that optimized all metrics simultaneously since 1.23 minimized the RMSE to 0.002 but the errors in R_2' and dCBV were both approximately -5%, while 1.14

minimized the percent error in R_2' and dCBV to within ± 0.5% but the RMSE was approximately 0.003.

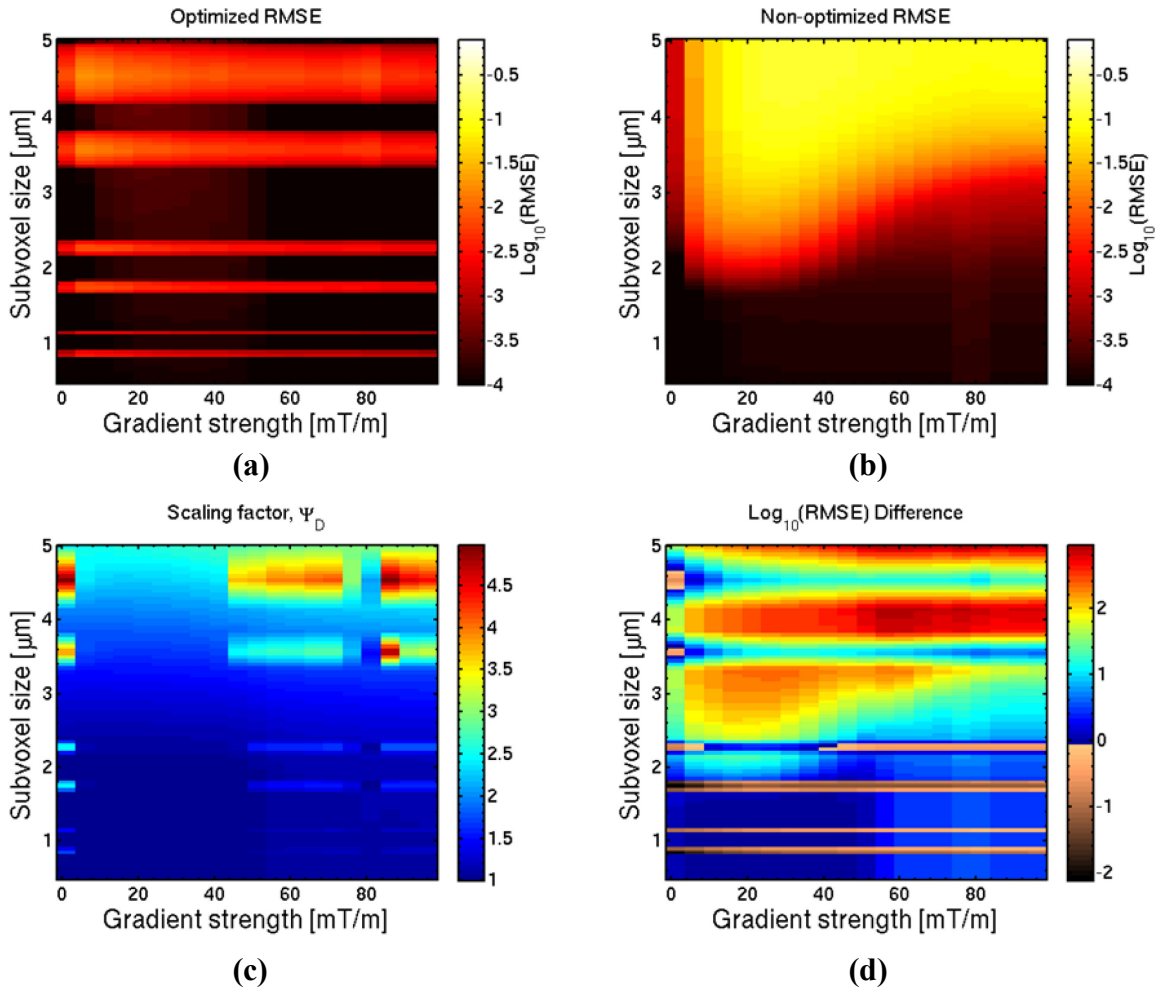

Figure 4.11: The minimized RMSE when the diffusion scaling factor, ψ_D, was optimized (a) and the corresponding RMSE obtained with no scaling (b) for D = 0.7 µm^2/ms. The map of ψ_D which minimized the RMSE in (a) is shown in (c). The difference (b) – (a) is shown in (d). Negative values in (d) are displayed in black to tan colours (where optimization failed) and positive values are displayed in blue to red colours (where optimization succeeded). Note that it is actually $\log_{10}$(RMSE) that is plotted in (a) and (b) and that difference in (d).

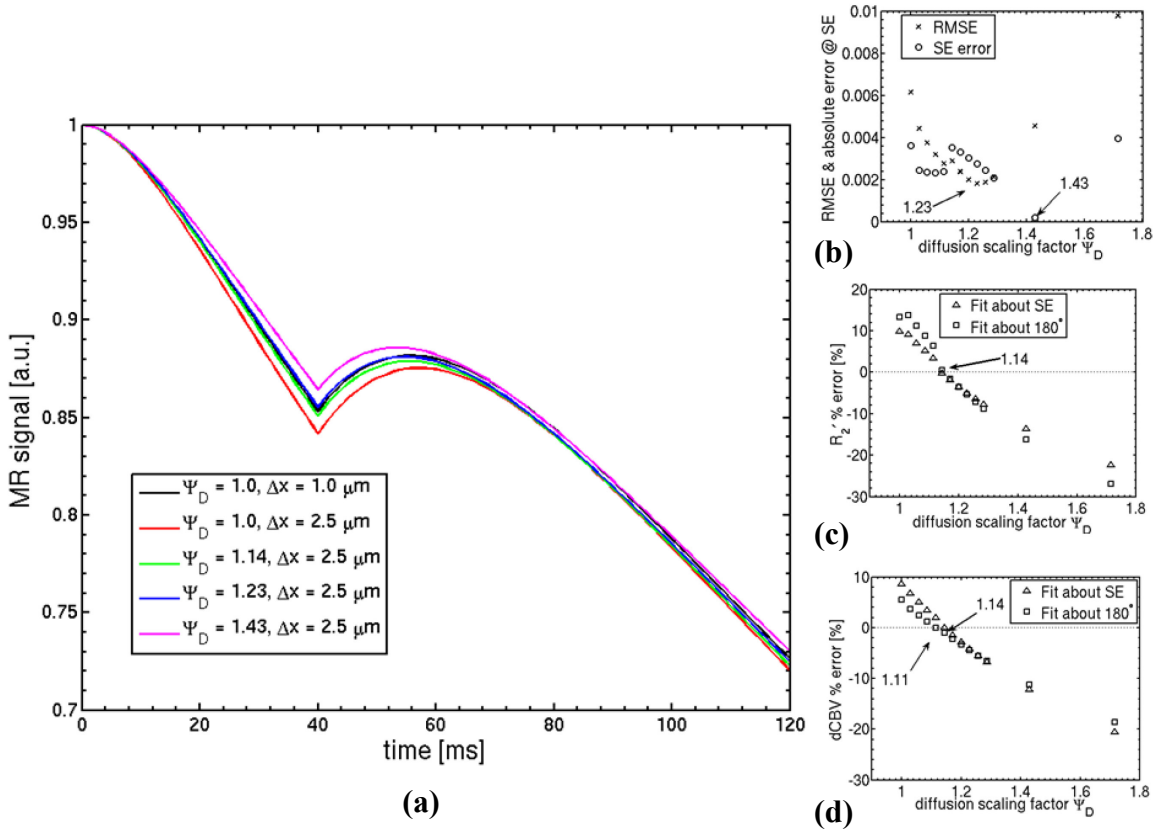

Figure 4.12: 3D optimization of ψ_D at 2.5 μm subvoxel size. Example time series of the target signal (D = 0.7 μm^2/ms, ψ_D = 1.0, and 1.0 μm subvoxels) and test signals with varying values of ψ_D (a). The RMSE and absolute error at the SE are shown in (b) for varying values of ψ_D. The percent difference in R_2' and dCBV are shown in (c) and (d) for varying values of ψ_D and fit either about the SE or about the refocusing pulse. The arrows and text in (b) – (d) indicate the particular values of ψ_D that minimized the metrics of interest.

Chapter 5 Discussion

Simulations in MRI have been invaluable for furthering our understanding of the technology and the biophysical principles underlying its contrast mechanisms. Throughout this thesis, one such method – deterministic simulation of the transverse magnetization – has been thoroughly validated for 3D simulations of a voxel. Validation experiments consisted of simulations with and without the modelling of molecular diffusion and with and without blood vessels present in the voxel. In all cases, the effect of the simulation subvoxel size was investigated.

When not including diffusion, the analytical theory of signal behaviour of blood vessel networks in the static dephasing regime from Yablonskiy and Haacke [60] was tested. This was done by checking the accuracy of the predictions made by the Yablonskiy and Haacke theory and examining how those predictions depended on the number of vessels present in the voxel.

More emphasis, however, was put on assessing simulations including diffusion. The model of diffusion as a blurring process, proposed by Bandettini and Wong [22], was

validated in 1D using a solution from Stejskal and Tanner [65] to the Bloch-Torrey equation with a constant linear gradient applied along one dimension. Using the RMSE and the error at the SE as the metrics of comparison, the simulated signals were compared with theory as D, time increment, TE, subvoxel size, and gradient strength were varied. Afterwards, the effects of subvoxel size and blood oxygen saturation were examined on 3D microvascular networks with simulations including diffusion. Finally, efforts to scale the diffusion coefficient in order to optimize simulations with large subvoxel sizes were carried out in 1D and tested in 3D.

The results from the simulations without diffusion are discussed here first followed by a discussion of the results including diffusion as well as general comments on the vascular model used with these deterministic simulations.

5.1 Simulations with Diffusion

5.1.1 Effect of Subvoxel Size

Varying the subvoxel size of eight different microvascular networks revealed very little dependence on the resolution for the simulations even up to a subvoxel size of 10 μm. This was for networks with a minimum vessel diameter of 2.78 μm. This, combined with the fact that the RMSE increased as the perturber strength increased (or as S_bO_2 decreased; Figure 4.1b), suggests that changing the subvoxel size only subtly altered the frequency spectrum but enough so that the higher degree of dispersion at increased perturber strength was less reliably reproduced. Considering this and that the perturber strength is also linearly proportional to B_0, one can extrapolate these results to predict that higher field strengths would require smaller subvoxel sizes.

5.1.2 Yablonskiy and Haacke Theory

Although not necessarily physically realistic, neglecting diffusion can be desirable because it can greatly simplify the analysis of complex systems. This was how

Yablonskiy and Haacke [60] approached the problem of signal behaviour from a network of blood vessels. Deterministic simulations provided an ideal method for validating this theory since, without diffusion, the simulations could easily satisfy the conditions required by it, including infinitely long, randomly oriented and homogeneously distributed vessels modelled as cylinders, no IV signal, system in the SDR (i.e. no diffusion), and large numbers of vessels.

The simulations without diffusion were found to be in very good agreement with the theoretically predicted R_2' and dCBV (Figure 4.2). For any given dCBV, the relative errors in R_2' and dCBV both followed a similar trend where they first increased with S_bO_2 and then proceeded to decrease. One explanation for this behaviour is that the perturber strength was affecting the simulation accuracy, as described in the previous section, but, simultaneously, the number of data points included in the linear fits to the time series changed as the perturber strength changed since the characteristic time, t_c, required to reach the asymptotic behaviour is inversely proportional to the perturber strength (see Eqs. (2.43) and (2.44)). Put another way, although the simulation accuracy increased as the perturber strength decreased, the window of time during which the simulation exhibited linear exponential behaviour shrunk, resulting in fewer data points for fitting the decay and a less accurate fit.

Furthermore, some of the error in the estimates of R_2' and dCBV would be attributable to systematic error that was shown to exist when fitting the analytical time series (Figure 4.3). The root cause of this error should be further explored but could be due to the assumption of the shift from quadratic exponential decay to linear exponential decay after $1.5t_c$ (Eq. (2.44)). Presumably, if more time points were included in the fits by increasing TE and the simulation time period, the fitted values would more closely match theory.

Another test of the Yablonskiy and Haacke theory was performed by Klassen and Menon [23] also using 3D deterministic simulations. They performed the same linearity test between the standard deviations of the relative errors of R_2' and dCBV vs. $1/\sqrt{N_{ves}}$. For R_2' they found a constant of proportionality of (54 ± 3)% with a coefficient of

determination $R^2 = 0.85$ and for dCBV they found a constant of proportionality of (35 ± 2)% with $R^2 = 0.85$. These were for simulations at 4 T with an S_bO_2 of 0.50 and Hct of 0.4, which at 3 T, using Eq.(2.43), corresponded to an S_bO_2 of 0.33 when Hct was 0.42 (the same B_0 and Hct used in this study). Their constants of proportionality were still much lower than the ones found in this study (Table 4.1), however, this was not too surprising since their TE was 90 ms compared to 80 ms here. Nevertheless, both studies found high R^2 values (0.85 for Klassen and Menon and 0.68 to 0.89 here), showing agreement with the strong assumption of large numbers of vessels underpinning the theory.

The applicability of the Yablonskiy and Haacke theory is limited though since it is strongly dependent on there being a large number of vessels occupying a negligible volume of tissue, that the vessels are completely randomly oriented, and perhaps most importantly, that the system is in the static dephasing regime. The only factor over which we, the experimenter, have control for determining whether or not the static dephasing regime applies is the field strength[7] since moving to higher field strengths increases $\delta\omega$ and therefore so too the likelihood that $\delta\omega \cdot \tau_D \gg 1$.

5.2 Simulations with Diffusion

5.2.1 Effect of Subvoxel Size

For a given value of D, the subvoxel size and time step must be judiciously chosen in order for the diffusion kernel not to behave like a delta function and not to span too large a distance such that edge effects start to occur even with an unsampled boundary. By performing SE simulations on a homogeneous 1D voxel that were *independent of field strength*, these simulation parameters were controlled for and assessed using primarily the RMSE but also the error at the SE. The error at the SE was of particular interest for several reasons: i) refocusing the spins allowed for a larger dynamic range of signal

[7] To a lesser extent, one could also try to pharmacologically decrease S_bO_2; however, when kept within physically safe limits, this decrease would be much less significant than increasing the field strength.

amplitudes to be simulated, ii) residual errors that propagated and added throughout the simulation were amplified and thus more apparent, and iii) practically speaking, the SE is typically the time point of interest in SE sequences.

It was found using the 1D simulations (Figure 4.9) and corroborated in 3D (Figure 4.10), that for a D equal to 0.7 $\mu m^2/ms$, the subvoxel size should be less than 2 μm. Using D = 0.7 $\mu m^2/ms$ was found to put the strictest constraints on the simulation accuracy (Figure 4.5) so using a larger value for D would allow for marginally larger subvoxels to be used considering the typical range of diffusion coefficients in GM is ~ 0.7 – 1.2 $\mu m^2/ms$ [66-69]. In the 2D vessel network simulations originally performed by Bandettini and Wong [22], they made the subvoxel size vary in proportion to the vessel diameter and dCBV being used. This technique allowed for the smallest capillaries to be sampled with relatively small subvoxels and the larger vessels to be sampled at lower resolutions. Since the simulation accuracy depends on both the subvoxel size and the gradient strength, this technique works very well since capillaries produce the largest gradients and are also sampled at higher resolution. On the other hand, Klassen and Menon's 3D simulations used values of D ranging from 0 up to 2.5 $\mu m^2/ms$ with a 5.85 μm subvoxel size and 1.0 ms time step [23]. The 1D and 3D simulations performed here showed that greater than 5 μm is far too large to accurately model the diffusion process – even at 4 T – and could result in relative errors for R_2' on the order of 100% (Figure 4.10).

Requiring such small subvoxels places exponentially larger demands on processor time and memory. For this reason, simulations were performed with 0.5 mm voxels in order to decrease the total matrix size; however, typical voxel dimensions in functional imaging are on the order of 1 – 3 mm. Christen, et al. [28] approached this issue by simulating multiple 0.2 mm voxel units and combining the complex MR signals from each of them into a larger composite voxel as if all of the voxel units had been arranged in a grid. Although this does not necessarily decrease the simulation time it does alleviate the memory demands. It is not clear though if their simulation validations were done on a single voxel unit or on a composite voxel. Having seen the boundary effects resulting from the convolution operations (Figure 4.4), this would be an important issue needing to be addressed when combining signals from multiple, supposedly neighbouring, voxel

units. Due to the random nature of the vessels and field offsets, it is possible that the edge effects would be negligible but in the case of an applied linear gradient, continuity of the gradient would be essential.

5.2.2 Scaling the Diffusion Coefficient

In the homogeneous 1D voxels, optimization of the diffusion scaling factor, ψ_D, proved capable of improving the RMSE by close to three orders of magnitude in some cases (Figure 4.11). In other cases, optimization failed, indicating that the optimization constraints and/or algorithm could be improved. As expected, the optimized ψ_D increased with increasing subvoxel size to compensate for the delta function-like behaviour that emerged as the subvoxel size was increased.

The optimized ψ_D was also dependent on the gradient strength – generally increasing as the gradient strength increased. This makes transitioning the optimized value from 1D to 3D simulations more challenging as there are non-linear gradients present in vessel networks which are themselves dependent on physiological factors such as Hct and S_bO_2. It may, however, be possible to obtain a characteristic gradient strength, similar to the characteristic frequency (Eq. (2.43)), which characterizes the vessel gradients. This gradient strength would presumably be dependent somehow on the distribution of vessel diameters and would, therefore, be easier to study using voxels composed of vessels with identical diameters. Determining this dependence would be very useful and, in addition to furthering our understanding of MR-vascular network interactions, it would eliminate the need to semi-manually seek out the best value for ψ_D in 3D.

Which metric will end up being the most useful for optimizing ψ_D in 3D vessel networks is still not clear. From the results presented in Figure 4.12, minimization of the error in R_2' and dCBV seems promising because, while optimizing the physical parameters of interest, it also produced an RMSE that was not significantly worse than the absolute minimized RMSE (0.003 vs. 0.002, respectively). On the contrary, minimizing the RMSE resulted in significantly worse errors on the estimates of R_2' and

dCBV (~ -5% vs. ± 0.5%, respectively). These results hold for only a single vessel network with a single set of simulation parameters, necessitating a more thorough investigation into the general applicability of the method.

If, ultimately, optimizing ψ_D is not practicable with microvascular networks, it may still find value in applications with linear or near-linear gradients, such as with larger blood vessels.

5.2.3 Vessel Models

In this thesis, as in most studies using deterministic simulations, vessel networks were modelled as randomly oriented cylinders of infinite extent with free permeability to water. Clearly these assumptions are not entirely realistic but it was not a goal of this thesis to assess their validity. Nevertheless, determining what effect these assumptions have on the simulation outcomes compared to more realistic models will be necessary for the simulations to gain widespread acceptance.

The Effect of Vascular Permeability

Boxerman, et al. [21] examined the effects of vessel permeability to water on MC simulations, varying it between zero permeability, physiological permeability, and free permeability. While the resulting differences between impermeable vessels and physiological permeability were negligible, simulations performed with free permeability displayed some marked differences from the others: changes in ΔR_2 peaked at approximately +20% for vessels with 6 μm radii and changes in ΔR_2^* dipped down to as low as -33% for vessels with 1 μm radii. While these relative differences may seem quite high, the absolute differences were very low, being on the order of 0.25 s^{-1}; furthermore, for a realistic distribution of vessels with a range of vessel radii, the net differences would be even less. Their studies were done at 1.5 T with an IV-EV susceptibility difference of 1.0×10^{-7} arising from a vascular concentration of 3.6 mM Gd-DTPA. As a result, the product $B_0 \cdot \Delta\chi$ from their studies and from the simulations performed here at 3 T using $S_bO_2 = 0.6$ and Hct = 0.42 were very similar (1.5×10^{-7} T vs. 1.3×10^{-7} T, respectively).

Sources of Intravascular Susceptibility Perturbation

Another shortcoming of the infinite cylinder model is that it does not accurately depict the sources of susceptibility inhomogeneity in the IV space, i.e. red blood cells and plasma. Using MC simulations, Martindale, et al. [24] modelled the IV perturbations from red blood cells by randomly distributing spherical perturbers within cylindrical vessels to a desired Hct. They found that for a single vessel, the IV signal phase as a function of vessel angle was very similar for the infinite cylinder and spherical perturber models; however, the normalized IV signal magnitude varied significantly as a function of vessel angle for the spherical perturber model with the simulation settings tested whereas the infinite cylinder model produces no deviation from unity since it generates a uniform phase shift throughout (Eq. (2.36)). Although their work did not show the discrepancy that may exist in the signal for an entire vessel network (IV + EV), the minimal volume occupied by the vessels would ensure that the effect is not too pronounced plus the long-range perturbations caused by neighbouring vessels would lead to some decay of the IV signal, although not to the extent observed with spherical perturbers. This could lead one to introduce a modulation factor to the IV signal for each vessel or, instead, directly model spherical perturbers, which would be feasible in deterministic simulations and more accurate. It's not clear though if the computational cost of including spherical perturbers would be worth the improvements in signal accuracy.

Infinite Cylinder Model vs. Realistic Vascular Model

Finally, modelling vessels as infinite cylinders is extremely convenient and efficient but not necessarily realistic (especially depending on the voxel size). Marques and Bowtell [70] examined this by comparing the infinite cylinder model to a realistic vascular model obtained from scanning electron microscopy measurements of the terminal vascular bed in the superficial cortex of the rat. In the realistic vascular model, vessel segments were still modelled as cylinders, however, the model gave the coordinates of the different nodes of the vasculature and the radii of the cylinders connecting those nodes. Field offsets for the realistic vascular model could no longer be computed analytically by Eq. (2.36) since the cylinders were of finite length, instead, Fourier-based method based on

the susceptibility map were used [71]. Simulations of the transverse magnetization were performed by numerically solving the Bloch-Torrey equation using finite element methods. They found no significant differences between the infinite cylinder model and the realistic vascular model in terms of the frequency offset histograms, ΔR_2, and ΔR_2^*. Their studies were performed using voxel widths of only 150 μm, so it remains to be seen how significant the differences are when larger voxels are used.

While it is important to understand that the models used in the simulations are only approximations of what occurs in reality, when performed within the proper bounds, the *trends* that are observed in the simulations are still very similar between different models; hence, one can still gain a great deal of information from the simulations and apply them to realistic physiology regardless of whether or not what they model is a perfect representation of nature.

Chapter 6 Conclusion

6.1 Summary

In an effort to fill in the existing gap in the MR literature, this thesis has extensively studied the fundamental properties and assumptions underpinning 3D deterministic simulations of the MRI signal. Analysis was divided into those simulations including molecular diffusion and those not including diffusion due to the leap in complexity between the two.

There were three principal findings from this study: 1) in the absence of diffusion, subvoxel size was *not* such a crucial factor and it could even be larger than the smallest field perturber size without significantly affecting the results; 2) in the presence of diffusion, subvoxel size *was* a crucial factor and it needed to be sufficiently high depending on the rest of the simulation parameters in order for the simulations to be accurate; and 3) optimization of a diffusion scaling factor for simulating with larger subvoxels was feasible when careful attention was paid to the simulation parameters.

The first finding, that the subvoxel size can be relatively large in the absence of diffusion, was determined by simulating the SE time series for different microvascular networks while progressively increasing the subvoxel size. Using up to 10 μm subvoxels showed no significant adverse effects compared to 1 μm subvoxels. Implications of this result are that larger, more realistic voxel sizes can be used without significantly increasing CPU time and memory demands, allowing for a wide range of phenomena in the static dephasing regime to be investigated. These simulations permitted the verification of the Yablonskiy and Haacke [60] theory of signal behaviour from a vascular network in the SDR, where good agreement between theory and simulation was found.

The second finding, that the subvoxel size had a major impact on the simulation outcomes when including molecular diffusion, was established first in 1D simulations that were independent of the field strength and vasculature and later verified in 3D microvascular simulations. The subvoxel size must therefore be meticulously chosen; one way of doing this is to perform the 1D simulations described in Sect. 3.3.1 with the desired simulation parameters while independently varying the subvoxel size and linear gradient strength. The RMSE and the error at the SE then provide quantitative tools for determining a sufficient subvoxel size for simulating to a desired accuracy.

Lastly, decreasing simulation time by using larger subvoxels showed promise when the diffusion coefficient was corrected for by an optimized scaling factor, ψ_D. By optimizing ψ_D for large subvoxel simulations in 1D, the RMSE could be improved by orders of magnitude over non-optimized simulations. The optimized ψ_D was both subvoxel size and gradient strength-dependent and therefore not so readily transferable to 3D vascular simulations; however, further investigation into optimization in 3D would be warranted since the potential benefits are vast.

6.2 Future Work

Many different properties of deterministic simulations were examined here but before the simulations can be put to meaningful use to gain insights into quantitative fMRI, some

more validation is required and the addition of some minor changes would make the simulations even more powerful.

In the simulations performed here, IV signal was always included when diffusion was being modelled. However, in some fMRI applications, it is advantageous to null the IV signal using flow dephasing gradients since IV signal can decrease the overall spatial specificity of the signal [72-74]. Modelling IV nulling in deterministic simulations is not as trivial as it is for MC simulations or analytical equations. The reason for this is that the model of free permeability inherent in isotropic blurring leads to increased signal loss in the EV areas surrounding vessels since EV signal is irretrievably lost to the IV space when convolved with the diffusion kernel. For this reason, the effect of IV nulling on the EV signal needs to be characterized. If EV signal losses become too pronounced, additional measures will have to be taken to reverse them, such as using a mask that would cause the diffusion kernel to spatially vary in the presence of vessels.

The power of the simulations and the range of their applications could be extended by incorporating some minor adjustments into them. First, as discussed in Sect. 5.2.3, the IV signal is not properly modelled by the infinite cylinder model and would be better modelled by a spherical perturber model [24]. This change would add time to the initial calculation of the field offset maps since more perturbation sources would be added, however, the runtime of the subsequent time series simulations would not be affected. Second, to create a less restricted picture of the vasculature, instead of applying a single oxygen saturation, a range of oxygen saturations could be applied to the vessel network, with each vessel or class of vessels (arterioles, capillaries, venules) taking on a unique value.

Finally, it is envisaged that the simulations will be applied to the evaluation of fMRI calibration techniques. Previous comparisons of calibration techniques have been *in vivo*, where only the *precision* of the techniques can be quantitatively compared since the ground truth calibration constants cannot be known [47, 75]. Simulations provide an excellent test bed for calibration since the physiological ground truth is already known and, therefore, the *accuracy* of the calibration methods can be quantitatively assessed. Blockley, et al. [29] conducted a comparison of hypercapnic, hyperoxic, and R_2'-based

calibration using an analytical model of the BOLD signal but, as previously discussed, analytical models need to incorporate many approximations and are therefore not as accurate. It is expected that deterministic simulations will be able to put better constraints on the calibration techniques than analytical models due to their low level control over physiological parameters.

Overall, deterministic simulations have great potential for use in MR studies: they provide accurate simulations of the MR signal in the microvasculature while delivering output variability that analytical solutions cannot produce and reducing the runtime required by MC simulations.

Bibliography

[1] V. R. Fuchs and H. C. Sox, Jr., "Physicians' views of the relative importance of thirty medical innovations," *Health Aff (Millwood),* vol. 20, pp. 30-42, Sep-Oct 2001.

[2] M. Carandini, "From circuits to behavior: a bridge too far?," *Nat Neurosci,* vol. 15, pp. 507-9, Apr 2012.

[3] S. Ogawa, D. W. Tank, R. Menon, J. M. Ellermann, S. G. Kim, H. Merkle, and K. Ugurbil, "Intrinsic signal changes accompanying sensory stimulation: functional brain mapping with magnetic resonance imaging," *Proc Natl Acad Sci U S A,* vol. 89, pp. 5951-5, Jul 1 1992.

[4] K. K. Kwong, J. W. Belliveau, D. A. Chesler, I. E. Goldberg, R. M. Weisskoff, B. P. Poncelet, D. N. Kennedy, B. E. Hoppel, M. S. Cohen, R. Turner, and et al., "Dynamic magnetic resonance imaging of human brain activity during primary sensory stimulation," *Proc Natl Acad Sci U S A,* vol. 89, pp. 5675-9, Jun 15 1992.

[5] P. A. Bandettini, E. C. Wong, R. S. Hinks, R. S. Tikofsky, and J. S. Hyde, "Time course EPI of human brain function during task activation," *Magn Reson Med,* vol. 25, pp. 390-7, Jun 1992.

[6] R. B. Buxton, "Interpreting oxygenation-based neuroimaging signals: the importance and the challenge of understanding brain oxygen metabolism," *Front Neuroenergetics,* vol. 2, pp. 1-16, 2010.

[7] R. B. Buxton, K. Uludag, D. J. Dubowitz, and T. T. Liu, "Modeling the hemodynamic response to brain activation," *Neuroimage,* vol. 23 Suppl 1, pp. S220-33, 2004.

[8] M. J. Donahue, J. U. Blicher, L. Ostergaard, D. A. Feinberg, B. J. MacIntosh, K. L. Miller, M. Gunther, and P. Jezzard, "Cerebral blood flow, blood volume, and oxygen metabolism dynamics in human visual and motor cortex as measured by whole-brain multi-modal magnetic resonance imaging," *J Cereb Blood Flow Metab,* vol. 29, pp. 1856-66, Nov 2009.

[9] V. E. Griffeth and R. B. Buxton, "A theoretical framework for estimating cerebral oxygen metabolism changes using the calibrated-BOLD method: modeling the effects of blood volume distribution, hematocrit, oxygen extraction fraction, and tissue signal properties on the BOLD signal," *Neuroimage,* vol. 58, pp. 198-212, Sep 1 2011.

[10] X. He and D. A. Yablonskiy, "Quantitative BOLD: mapping of human cerebral deoxygenated blood volume and oxygen extraction fraction: default state," *Magn Reson Med,* vol. 57, pp. 115-26, Jan 2007.

[11] R. D. Hoge, J. Atkinson, B. Gill, G. R. Crelier, S. Marrett, and G. B. Pike, "Investigation of BOLD signal dependence on cerebral blood flow and oxygen consumption: the deoxyhemoglobin dilution model," *Magn Reson Med,* vol. 42, pp. 849-63, Nov 1999.

[12] P. Tian, I. C. Teng, L. D. May, R. Kurz, K. Lu, M. Scadeng, E. M. Hillman, A. J. De Crespigny, H. E. D'Arceuil, J. B. Mandeville, J. J. Marota, B. R. Rosen, T. T. Liu, D. A. Boas, R. B. Buxton, A. M. Dale, and A. Devor, "Cortical depth-specific microvascular dilation underlies laminar differences in blood oxygenation level-dependent functional MRI signal," *Proc Natl Acad Sci USA,* vol. 107, pp. 15246-51, Aug 24 2010.

[13] K. Uludag, D. J. Dubowitz, E. J. Yoder, K. Restom, T. T. Liu, and R. B. Buxton, "Coupling of cerebral blood flow and oxygen consumption during physiological activation and deactivation measured with fMRI," *Neuroimage,* vol. 23, pp. 148-55, Sep 2004.

[14] S. A. Rombouts, R. Goekoop, C. J. Stam, F. Barkhof, and P. Scheltens, "Delayed rather than decreased BOLD response as a marker for early Alzheimer's disease," *Neuroimage,* vol. 26, pp. 1078-85, Jul 15 2005.

[15] S. Amemiya, A. Kunimatsu, N. Saito, and K. Ohtomo, "Impaired hemodynamic response in the ischemic brain assessed with BOLD fMRI," *Neuroimage,* vol. 61, pp. 579-90, Jul 2 2012.

[16] K. C. Mazzetto-Betti, R. F. Leoni, O. M. Pontes-Neto, A. C. Santos, J. P. Leite, A. C. Silva, and D. B. de Araujo, "The stability of the blood oxygenation level-dependent functional MRI response to motor tasks is altered in patients with chronic ischemic stroke," *Stroke,* vol. 41, pp. 1921-6, Sep 2010.

[17] C. J. Gauthier, C. Madjar, F. B. Tancredi, B. Stefanovic, and R. D. Hoge, "Elimination of visually evoked BOLD responses during carbogen inhalation: implications for calibrated MRI," *Neuroimage,* vol. 54, pp. 1001-11, Jan 15 2011.

[18] E. Kraft, W. Loichinger, M. Diepers, D. Lule, J. Schwarz, A. C. Ludolph, and A. Storch, "Levodopa-induced striatal activation in Parkinson's disease: a functional MRI study," *Parkinsonism Relat Disord,* vol. 15, pp. 558-63, Sep 2009.

[19] S. Ogawa, R. S. Menon, D. W. Tank, S. G. Kim, H. Merkle, J. M. Ellermann, and K. Ugurbil, "Functional brain mapping by blood oxygenation level-dependent contrast magnetic resonance imaging. A comparison of signal characteristics with a biophysical model," *Biophys J,* vol. 64, pp. 803-12, Mar 1993.

[20] J. L. Boxerman, P. A. Bandettini, K. K. Kwong, J. R. Baker, T. L. Davis, B. R. Rosen, and R. M. Weisskoff, "The intravascular contribution to fMRI signal change: Monte Carlo modeling and diffusion-weighted studies in vivo," *Magn Reson Med,* vol. 34, pp. 4-10, Jul 1995.

[21] J. L. Boxerman, L. M. Hamberg, B. R. Rosen, and R. M. Weisskoff, "MR Contrast Due to Intravascular Magnetic-Susceptibility Perturbations," *Magn Reson Med,* vol. 34, pp. 555-566, Oct 1995.

[22] P. A. Bandettini and E. C. Wong, "Effects of biophysical and physiologic parameters on brain activation-induced R2* and R2 changes: Simulations using a

deterministic diffusion model," *Int J Imaging Syst Technol,* vol. 6, pp. 133-152, 1995.

[23] L. M. Klassen and R. S. Menon, "NMR simulation analysis of statistical effects on quantifying cerebrovascular parameters," *Biophys J,* vol. 92, pp. 1014-21, Feb 1 2007.

[24] J. Martindale, A. J. Kennerley, D. Johnston, Y. Zheng, and J. E. Mayhew, "Theory and generalization of Monte Carlo models of the BOLD signal source," *Magn Reson Med,* vol. 59, pp. 607-18, Mar 2008.

[25] J. D. Dickson, T. W. Ash, G. B. Williams, S. G. Harding, T. A. Carpenter, D. K. Menon, and R. E. Ansorge, "Quantitative BOLD: the effect of diffusion," *J Magn Reson Imaging,* vol. 32, pp. 953-61, Oct 2010.

[26] T. Christen, B. Lemasson, N. Pannetier, R. Farion, C. Segebarth, C. Remy, and E. L. Barbier, "Evaluation of a quantitative blood oxygenation level-dependent (qBOLD) approach to map local blood oxygen saturation," *NMR Biomed,* vol. 24, pp. 393-403, Oct 19 2010.

[27] D. Pflugfelder, K. Vahedipour, K. Uludag, N. J. Shah, and T. Stocker, "On the numerically predicted spatial BOLD fMRI specificity for spin echo sequences," *Magn Reson Imaging,* vol. 29, pp. 1195-204, Nov 2011.

[28] T. Christen, G. Zaharchuk, N. Pannetier, R. Serduc, N. Joudiou, J. C. Vial, C. Remy, and E. L. Barbier, "Quantitative MR estimates of blood oxygenation based on T(2) *: A numerical study of the impact of model assumptions," *Magn Reson Med,* vol. 67, pp. 1458-68, May 2012.

[29] N. P. Blockley, V. E. Griffeth, and R. B. Buxton, "A general analysis of calibrated BOLD methodology for measuring CMRO2 responses: comparison of a new approach with existing methods," *Neuroimage,* vol. 60, pp. 279-89, Mar 2012.

[30] S. G. Waxman, "Chapter 2. Development and Cellular Constituents of the Nervous System," in *Clinical Neuroanatomy*, S. G. Waxman, Ed., 26 ed. New York: McGraw-Hill, 2010.

[31] D. U. Silverthorn, "Chapter 8: The Nervous System," in *Human physiology : an integrated approach*, 1 ed Upper Saddle River, N.J.: Prentice Hall, 1998.

[32] R. B. Buxton, *Introduction to functional magnetic resonance imaging : principles and techniques*, 2nd ed. Cambridge ; New York: Cambridge University Press, 2009.

[33] M. E. Raichle, A. M. MacLeod, A. Z. Snyder, W. J. Powers, D. A. Gusnard, and G. L. Shulman, "A default mode of brain function," *Proc Natl Acad Sci USA,* vol. 98, pp. 676-82, Jan 16 2001.

[34] P. T. Fox, M. E. Raichle, M. A. Mintun, and C. Dence, "Nonoxidative glucose consumption during focal physiologic neural activity," *Science,* vol. 241, pp. 462-4, Jul 22 1988.

[35] T. L. Davis, K. K. Kwong, R. M. Weisskoff, and B. R. Rosen, "Calibrated functional MRI: mapping the dynamics of oxidative metabolism," *Proc Natl Acad Sci USA,* vol. 95, pp. 1834-9, Feb 17 1998.

[36] R. B. Buxton, "Chapter 2: Cerebral blood flow and brain activation," in *Introduction to functional magnetic resonance imaging : principles and techniques*, 2nd ed Cambridge ; New York: Cambridge University Press, 2009.

[37] J. Andresen, N. I. Shafi, and R. M. Bryan, Jr., "Endothelial influences on cerebrovascular tone," *J Appl Physiol,* vol. 100, pp. 318-27, Jan 2006.
[38] H. Ito, I. Kanno, C. Kato, T. Sasaki, K. Ishii, Y. Ouchi, A. Iida, H. Okazawa, K. Hayashida, N. Tsuyuguchi, K. Ishii, Y. Kuwabara, and M. Senda, "Database of normal human cerebral blood flow, cerebral blood volume, cerebral oxygen extraction fraction and cerebral metabolic rate of oxygen measured by positron emission tomography with 15O-labelled carbon dioxide or water, carbon monoxide and oxygen: a multicentre study in Japan," *Eur J Nucl Med Mol Imaging,* vol. 31, pp. 635-43, May 2004.
[39] P. C. van Zijl, S. M. Eleff, J. A. Ulatowski, J. M. Oja, A. M. Ulug, R. J. Traystman, and R. A. Kauppinen, "Quantitative assessment of blood flow, blood volume and blood oxygenation effects in functional magnetic resonance imaging," *Nat Med,* vol. 4, pp. 159-67, Feb 1998.
[40] B. Weber, A. L. Keller, J. Reichold, and N. K. Logothetis, "The microvascular system of the striate and extrastriate visual cortex of the macaque," *Cereb Cortex,* vol. 18, pp. 2318-30, Oct 2008.
[41] F. Lauwers, F. Cassot, V. Lauwers-Cances, P. Puwanarajah, and H. Duvernoy, "Morphometry of the human cerebral cortex microcirculation: general characteristics and space-related profiles," *Neuroimage,* vol. 39, pp. 936-48, Feb 1 2008.
[42] S. Hirsch, J. Reichold, M. Schneider, G. Szekely, and B. Weber, "Topology and hemodynamics of the cortical cerebrovascular system," *J Cereb Blood Flow Metab,* Apr 4 2012.
[43] R. L. Grubb, Jr., M. E. Raichle, J. O. Eichling, and M. M. Ter-Pogossian, "The effects of changes in PaCO2 on cerebral blood volume, blood flow, and vascular mean transit time," *Stroke,* vol. 5, pp. 630-9, Sep-Oct 1974.
[44] M. F. Perutz, "Relation between structure and sequence of haemoglobin," *Nature,* vol. 194, pp. 914-7, Jun 9 1962.
[45] L. Pauling and C. D. Coryell, "The Magnetic Properties and Structure of Hemoglobin, Oxyhemoglobin and Carbonmonoxyhemoglobin," *Proc Natl Acad Sci USA,* vol. 22, pp. 210-6, Apr 1936.
[46] C. Schwarzbauer and R. Deichmann, "Vascular component analysis of hyperoxic and hypercapnic BOLD contrast," *Neuroimage,* vol. 59, pp. 2401-12, Feb 1 2012.
[47] C. I. Mark, J. A. Fisher, and G. B. Pike, "Improved fMRI calibration: precisely controlled hyperoxic versus hypercapnic stimuli," *Neuroimage,* vol. 54, pp. 1102-11, Jan 15 2011.
[48] J. J. Chen and G. B. Pike, "BOLD-specific cerebral blood volume and blood flow changes during neuronal activation in humans," *NMR Biomed,* vol. 22, pp. 1054-62, Dec 2009.
[49] C. I. Mark and G. B. Pike, "Indication of BOLD-specific venous flow-volume changes from precisely controlled hyperoxic vs. hypercapnic calibration," *J Cereb Blood Flow Metab,* vol. 32, pp. 709-19, Apr 2012.
[50] P. A. Chiarelli, D. P. Bulte, R. Wise, D. Gallichan, and P. Jezzard, "A calibration method for quantitative BOLD fMRI based on hyperoxia," *Neuroimage,* vol. 37, pp. 808-20, Sep 1 2007.

[51] C. J. Gauthier and R. D. Hoge, "A generalized procedure for calibrated fMRI incorporating hyperoxia and hypercapnia," in *Intl Soc Mag Reson Med 19*, Montreal, 2011, p. 772.
[52] N. P. Blockley, V. E. Griffeth, and R. B. Buxton, "Can the calibrated BOLD scaling factor M be estimated just from R2' in the baseline state without administering gases," in *Intl Soc Mag Reson Med 19*, Montreal, 2011, p. 768.
[53] D. Le Bihan and P. J. Basser, "Chapter 1: Molecular Diffusion and Nuclear Magnetic Resonance," in *Diffusion and perfusion magnetic resonance imaging applications to functional MRI*, D. Le Bihan, Ed., ed New York: Raven Press, 1995, pp. xxi, 374 p.
[54] A. Einstein, *Investigations on the theory of the Brownian movement*. New York: Dover Publications, 1956.
[55] D. Le Bihan, R. Turner, and N. Patronas, "Chapter 8: Diffusion MR imaging in normal brain and in brain tumors," in *Diffusion and perfusion magnetic resonance imaging applications to functional MRI*, D. Le Bihan, Ed., ed New York: Raven Press, 1995, pp. xxi, 374 p.
[56] P. T. Callaghan, "Chapter 6: The measurement of motion using spin echoes," in *Principles of nuclear magnetic resonance microscopy*, ed Oxford [England] ; New York: Oxford University Press, 1991, p. 492 p.
[57] H. Torrey, "Bloch Equations with Diffusion Terms," *Physical Review,* vol. 104, pp. 563-565, 1956.
[58] R. M. Weisskoff, C. S. Zuo, J. L. Boxerman, and B. R. Rosen, "Microscopic susceptibility variation and transverse relaxation: theory and experiment," *Magn Reson Med,* vol. 31, pp. 601-10, Jun 1994.
[59] J. M. Zhao, C. S. Clingman, M. J. Narvainen, R. A. Kauppinen, and P. C. van Zijl, "Oxygenation and hematocrit dependence of transverse relaxation rates of blood at 3T," *Magn Reson Med,* vol. 58, pp. 592-7, Sep 2007.
[60] D. A. Yablonskiy and E. M. Haacke, "Theory of NMR signal behavior in magnetically inhomogeneous tissues: the static dephasing regime," *Magn Reson Med,* vol. 32, pp. 749-63, Dec 1994.
[61] D. A. Yablonskiy, "Quantitation of intrinsic magnetic susceptibility-related effects in a tissue matrix. Phantom study," *Magn Reson Med,* vol. 39, pp. 417-28, Mar 1998.
[62] J. P. Wansapura, S. K. Holland, R. S. Dunn, and W. S. Ball, "NMR relaxation times in the human brain at 3.0 tesla," *J Magn Reson Imaging,* vol. 9, pp. 531-538, Apr 1999.
[63] W. M. Spees, D. A. Yablonskiy, M. C. Oswood, and J. J. H. Ackerman, "Water proton MR properties of human blood at 1.5 Tesla: magnetic susceptibility, T1, T2, T2*, and non-Lorentzian signal behavior," *Magn Reson Med,* vol. 45, pp. 533-542, 2001.
[64] H. Y. Carr and E. M. Purcell, "Effects of Diffusion on Free Precession in Nuclear Magnetic Resonance Experiments," *Physical Review,* vol. 94, pp. 630-638, 1954.
[65] E. O. Stejskal and J. E. Tanner, "Spin Diffusion Measurements: Spin Echoes in the Presence of a Time-Dependent Field Gradient," *Journal of Chemical Physics,* vol. 42, pp. 288-+, 1965.

[66] J. M. Ni, S. Chen, J. J. Liu, G. Huang, T. Z. Shen, and X. R. Chen, "Regional diffusion changes of cerebral grey matter during normal aging--a fluid-inversion prepared diffusion imaging study," *Eur J Radiol,* vol. 75, pp. 134-8, Aug 2010.

[67] R. J. Fox, K. Sakaie, J. C. Lee, J. P. Debbins, Y. Liu, D. L. Arnold, E. R. Melhem, C. H. Smith, M. D. Philips, M. Lowe, and E. Fisher, "A validation study of multicenter diffusion tensor imaging: reliability of fractional anisotropy and diffusivity values," *AJNR Am J Neuroradiol,* vol. 33, pp. 695-700, Apr 2012.

[68] J. F. Jansen, M. E. Kooi, A. G. Kessels, K. Nicolay, and W. H. Backes, "Reproducibility of quantitative cerebral T2 relaxometry, diffusion tensor imaging, and 1H magnetic resonance spectroscopy at 3.0 Tesla," *Invest Radiol,* vol. 42, pp. 327-37, Jun 2007.

[69] B. Benedetti, A. Charil, M. Rovaris, E. Judica, P. Valsasina, M. P. Sormani, and M. Filippi, "Influence of aging on brain gray and white matter changes assessed by conventional, MT, and DT MRI," *Neurology,* vol. 66, pp. 535-9, Feb 28 2006.

[70] J. P. Marques and R. W. Bowtell, "Using forward calculations of the magnetic field perturbation due to a realistic vascular model to explore the BOLD effect," *NMR Biomed,* vol. 21, pp. 553-65, Jul 2008.

[71] J. P. Marques and R. Bowtell, "Application of a fourier-based method for rapid calculation of field inhomogeneity due to spatial variation of magnetic susceptibility," *Concepts in Magnetic Resonance Part B-Magnetic Resonance Engineering,* vol. 25B, pp. 65-78, Apr 2005.

[72] H. An and W. Lin, "Impact of intravascular signal on quantitative measures of cerebral oxygen extraction and blood volume under normo- and hypercapnic conditions using an asymmetric spin echo approach," *Magn Reson Med,* vol. 50, pp. 708-16, Oct 2003.

[73] M. J. Donahue, H. Hoogduin, P. C. van Zijl, P. Jezzard, P. R. Luijten, and J. Hendrikse, "Blood oxygenation level-dependent (BOLD) total and extravascular signal changes and DeltaR2* in human visual cortex at 1.5, 3.0 and 7.0 T," *NMR Biomed,* vol. 24, pp. 25-34, Jan 2011.

[74] T. Q. Duong, E. Yacoub, G. Adriany, X. P. Hu, K. Ugurbil, and S. G. Kim, "Microvascular BOLD contribution at 4 and 7 T in the human brain: Gradient-echo and spin-echo fMRI with suppression of blood effects," *Magn Reson Med,* vol. 49, pp. 1019-1027, Jun 2003.

[75] C. J. Gauthier and R. D. Hoge, "Magnetic resonance imaging of resting OEF and CMRO(2) using a generalized calibration model for hypercapnia and hyperoxia," *Neuroimage,* vol. 60, pp. 1212-25, Apr 2 2012.